Journal of
South American
Earth Sciences

Including Mexico, Central America, The Caribbean and the Antarctic Peninsula

See the JOURNAL OF SOUTH AMERICAN
EARTH SCIENCES on the World Wide Web
http://www.elsevier.com/locate/jsames

The Aguilar pluton (23°12′ S–65°40′ W; NW Argentina): Petrological implications on the origin of the Late Jurassic intraplate magmatism in the Central Andes

CrossMark

Ricardo H. Omarini [a,*], Anna Gioncada [b], Luigina Vezzoli [c], Roberto Mazzuoli [b], Chiara Cristiani [d], Ricardo J. Sureda [a]

[a] Facultad de Ciencias Naturales, Universidad Nacional de Salta, CONICET-CIUNSA, Av. Bolivia 5150, Salta 4400, Argentina
[b] Dipartimento di Scienze della Terra, Università degli Studi di Pisa, Pisa, Italy
[c] Dipartimento di Scienza e Alta Tecnologia, Università dell'Insubria, Como, Italy
[d] Department Civil Protection of Italy – Volcanic Risk Service, Italy

ARTICLE INFO

ABSTRACT

The Late Jurassic Aguilar pluton is located in NW Argentina, about 300–400 Km east of the Tarapacá basin, representing the backarc basin linked to the Jurassic volcanic arc. This small-size and compositionally heterogeneous pluton intruded the metasedimentary rocks of the Ordovician Santa Victoria Group, along the Cobres-Salinas Grandes lineament. A revision of published geochemical data in the light of new field and petrological results, allows us to propose a model concerning the petrogenesis and emplacement mechanisms of Aguilar pluton and to discuss its geodynamic setting. The pluton is mainly composed of metaluminous and nearly peraluminous granitoids, showing the geochemical characteristics of ferroan granites. The volumetrically subordinate mafic rocks are both ne- and hy-normative, and their primary magmas were generated by partial melting of a pristine Proterozoic mantle. Aguilar rocks display a rather limited range in $({}^{87}Sr/{}^{86}Sr)_i$, compared to the entire rift-related plutonic suite, i.e., 0.703198–0.704601, and εNd_f from −1.06 to 3.82, calculated at 149 Ma. Fractional crystallization of mantle-derived magmas and crustal contamination processes explain the evolution to produce strongly silica-oversaturated magmas, which emplaced in the continental crust. The petrological data indicate that magma emplacement and cooling occurred at rather shallow depth. Multiple injections of magma batches into the magma chamber caused mingling and mixing processes early in the crystallization history. The Aguilar pluton is one of the several igneous complexes whose formation was associated with the extensional tectonics active during Late Jurassic-Early Cretaceous in NW Argentina. Based on the geological position and the igneous rocks affinity, we exclude that the Late Jurassic magmatism was generated in an orogenic setting and envisage that it was linked to the early extensional phase that preceded the Cretaceous continental rifting, related to the break–up of the South America-Africa continents.

1. Introduction

Since Early Mesozoic time, the Andean margin geodynamic evolution was characterized by the subsequent subduction of the Aluk, Farallon and Pacific oceanic plates under the South American continent (Zonenshayn et al., 1984; Jaillard et al., 1990; Scheuber et al., 1994, Fig. 1A). During the Late Jurassic-Early Cretaceous, the oblique convergence of the Aluk plate with the South American plate produced a transtensional-extensional tectonic regime along the continental margin, which favored the emplacement of a long-lived magmatic arc forming the present Coastal Cordillera (Fig. 1B). Arc magmatism began in the Coastal Cordillera at 180 Ma and lasted until 100 Ma, including the emplacement of large volumes of mafic lavas and coeval batholiths (Oliveros et al., 2006; Boekhout et al., 2012). The Jurassic-Early Cretaceous forearc realm is unknown because it was eroded during the on-going subduction (Rutland, 1971; Stern, 1991; Mpodozis and Ramos, 1990; Ramos, 2000, 2009). East of the magmatic arc, the extensional stress regime and the subsequent crustal thinning provided the space for the development of the continental-marine Tarapacá basin, that

* Corresponding author.
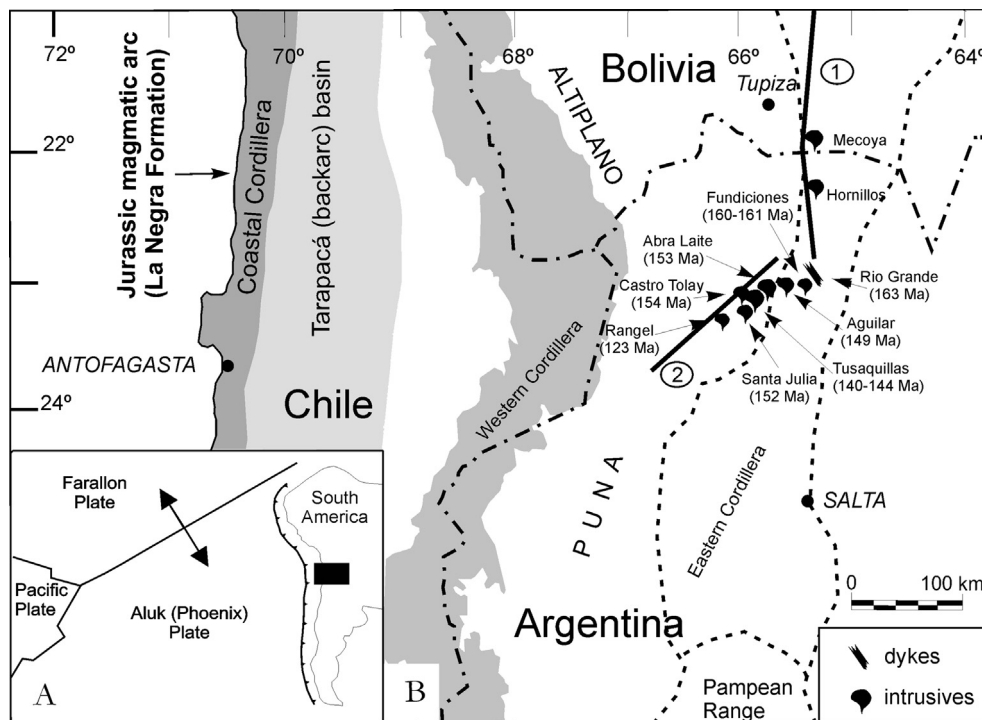*E-mail address:* rhomarini@arnet.com.ar (R.H. Omarini).

Fig. 1. A. Plate configuration of the southern Pacific in correspondence of the Central Andes at about 150 Ma, after Scheuber et al. (1994). B. Geological sketch of the southern Central Andes showing the location, in NW Argentina, of the Upper Jurassic-Lower Cretaceous plutons. The paleogeographic reconstruction of the Jurassic magmatic arc (Coastal Cordillera) and associated Tarapacá basin is after Printz et al. (1994). (1) El Condor lineament; (2) Cobres-Salinas Grandes lineament after Marquillas and Salfity (1988).

extends from 21° to 28°S. Many authors (Muñoz et al., 1988; Gröschke et al., 1988; Charrier and Muñoz, 1994; Printz et al., 1994; Jaillard et al., 2000) considered it as a backarc basin linked to the Jurassic magmatic arc (Fig. 1B). In the foreland, at 300–400 km east of the Tarapacá basin, between 18°S and 28°S, a widespread magmatism developed in an extensional tectonic regime in Late Jurassic-Early Cretaceous time, before the Cretaceous rift-related sedimentation of Salta Group (Marquillas and Salfity, 1988). The geodynamic setting of this magmatism is controversial. Viramonte et al. (1999) included it in the backarc magmatism of the Jurassic-Cretaceous active continental margin. More recently, based on geochronological and petrological data, the extensional tectonic phase responsible for this magmatic activity has been linked to the break-up of the South America-Africa continents (Cristiani et al., 2005).

The Late Jurassic-Early Cretaceous magmatic activity formed two discrete plutonic belts, roughly aligned along the El Condor and Cobres-Salinas Grandes lineaments (Fig. 1B) (Marquillas and Salfity, 1988). These belts include the Rangel, Castro Tolay, Santa Julia, Tusaquillas, Abra Laite, Aguilar, Fundiciones, Hornillos, and Mecoya plutons (about 163 to 123 Ma, Rubiolo, 1992; Menegatti, 2001; Cristiani, 2003; Zappettini, 2008; Hauser et al., 2010). The plutons show a great variety of rock compositions, ranging from metaluminous biotite or amphibole + biotite granitoids (70 vol%), to peraluminous biotite + muscovite ± garnet or cordierite granitoids (10 vol%) and gabbroic intrusions, syenitic differentiates, peralkaline granitoids and lamprophyres (20 vol%). Later, between 120 and 60 Ma, alkaline volcanic rocks prevail (basanite, trachyte, nephelinite, tephriphonolite, mugearite and alkali olivine basalts with lower crust and mantle xenoliths; Viramonte et al., 1999; Lucassen et al., 1999, 2005, 2007; Comin Chiaramonti et al., 2009). These Cretaceous volcanic rocks are intercalated with syn-rift deposits of the Salta Group (Salfity and Marquillas, 1994).

The focus of this paper is the Aguilar pluton (AG pluton hereafter), whose compositional heterogeneity and location at the eastern end of the plutonic belt provide the opportunity to study the origin and evolution of the Late Jurassic intraplate magmatism in NW Argentina (Fig. 1B). The geology of the AG pluton was presented in the early works of Hausen (1925), Spencer (1950), Turner (1970) and Lamfranco (1972). Isotopic and geochronological data, ranging from 200 Ma to 150 Ma, have been reported by Linares (1968), Stipanicic and Linares (1969), Halpern and Latorre (1973), Linares and Latorre (1975), Haschke et al. (2005), Cristiani (2003). Regional geological data related to the presence of lead-zinc mineralization have been given by Brodtkorb et al. (1978), Gemmell et al. (1992) and Sureda and Martin (1990). More recently, petrological and geochemical data have been reported by Cristiani et al. (2002, 2003, 2005) and Haschke et al. (2005). In this paper, we combine geochemical data reported in a previous paper (Cristiani et al., 2005) with new field, petrographic and mineralogical results, with the aim to define the petrogenetic processes and emplacement mechanisms of the AG pluton. Moreover, we discuss and compare the results with the available data on the coeval intrusions in the study area, and we propose a general tectono-magmatic model for the Late Jurassic-Early Cretaceous magmatism in NW Argentina.

2. Geology

The AG pluton is located in the Jujuy Province, NW Argentina (23°12′S, 65°40′W), near to the boundary between the morphostructural units of the Eastern Cordillera and Puna Plateau (Fig. 1B). The pluton crops out on an area of about 45 km^2 and shows a roughly ellipsoidal shape, with the major axis trending N–S along the eastern margin of the Aguilar Range (Fig. 2). The intrusive body is cut by the Eastern and Western Aguilar faults and the Quemado fault (Fig. 2). The Eastern Aguilar Fault is a reverse fault with
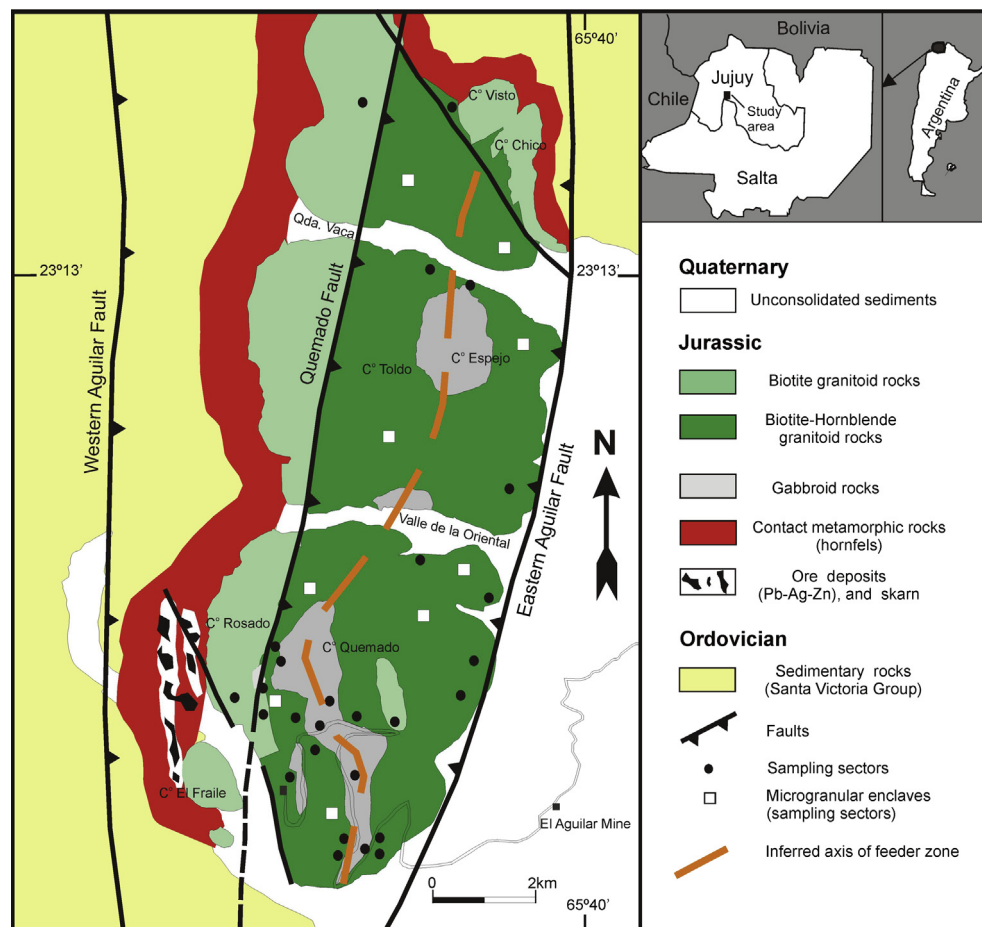
Fig. 2. Geological sketch map of the Aguilar pluton, showing the distribution of the main lithological facies and the sampling sites (geology modified after Lamfranco, 1972; Gemmell et al., 1992).

eastward vergence, probably linked to the detachment thrust of the Puna basement on the Eastern Cordillera morphostructural units (Drozdzwski and Mon, 1999). The Western Aguilar and the Quemado faults represent westward-verging reverse faults generated as a consequence of the regional shortening during the Andean compressional deformation (Cladouhos et al., 1994; Kley et al., 1999; Coutand et al., 2001). The compressional deformation uplifted the AG pluton through oppositely vergent, north-northeast striking thrust faults (Fig. 2), active at 17–12 Ma in the eastern border of the Puna plateau (Marrett and Strecker, 2000; Allmendinger and Zapata, 2000; Acocella et al., 2007).

The age of the Aguilar pluton was determined at 149.4 ± 1 Ma by Rb/Sr isochrone (Cristiani, 2003) and 150.4 ± 0.9 Ma by U/Pb on zircon (Haschke et al., 2005). A contact metamorphism aureole developed in the Ordovician sedimentary rocks surrounding the pluton in the western and northern sectors. These host rocks originally consisted of marine-platform sediments including sandstones, shales and limestones (Spencer, 1950). Moving away from the intrusion, the metamorphic facies range from pyroxene-hornfels (K-feldspar-cordierite-andalusite) to hornblende-hornfels and albite-epidote hornfels (Lamfranco, 1972; Brodtkorb et al., 1978). Several broad metasomatic skarn zones, bearing a calc-silicate assemblage (garnet, hedenbergite, johannsenite and vesu-vianite) and hosting sphalerite, galena and pyrite intercalated with carbonate and silicate gangue minerals, are present near to the contact with the plutonic body (Sureda and Martín, 1990; Gemmell et al., 1992). The Aguilar mine has been exploiting since 1930's

strata-bound Zn–Pb–Ag sulfide ores hosted by the Aguilar pluton contact aureole quartzites and hornfels. The ores are interpreted as sedimentary-exhalative stratiform deposits formed in the Ordovician marine sediments and later overprinted by contact metamorphism during the emplacement of the AG pluton (Gemmell et al., 1992).

The AG pluton mainly consists of granitoid rocks. Gabbroid rocks are dispersed in the central and southern sectors (cerro Quemado, valle de la Oriental, and cerro Espejo) of the pluton as massive bodies, enclaves and sill-like intrusions (Figs. 2 and 3).

3. Petrography

The AG pluton presents a rather large variety of rock types, which can be grouped into *granitoid-sienitoid* (hereafter granitoid l.s.) and *gabbroid* rocks. According to the modal classification of Streickeisen (1976), the *granitoid s.l.* rocks are mainly monzogranite and quartz-monzonite with subordinate quartz-syenite; the *gabbroid* rocks are monzodiorite and quartz-monzodiorite with minor diorite, gabbro and foid-gabbro (Fig. 4).

3.1. Granitoids l.s. rocks

These rocks present a great variability in colour from pale pink to grey and have medium-grained hypidiomorphic, heterogranular textures. The main mineral phases of the monzogranite are orthoclase, plagioclase, quartz, biotite, hornblende, with magnetite,
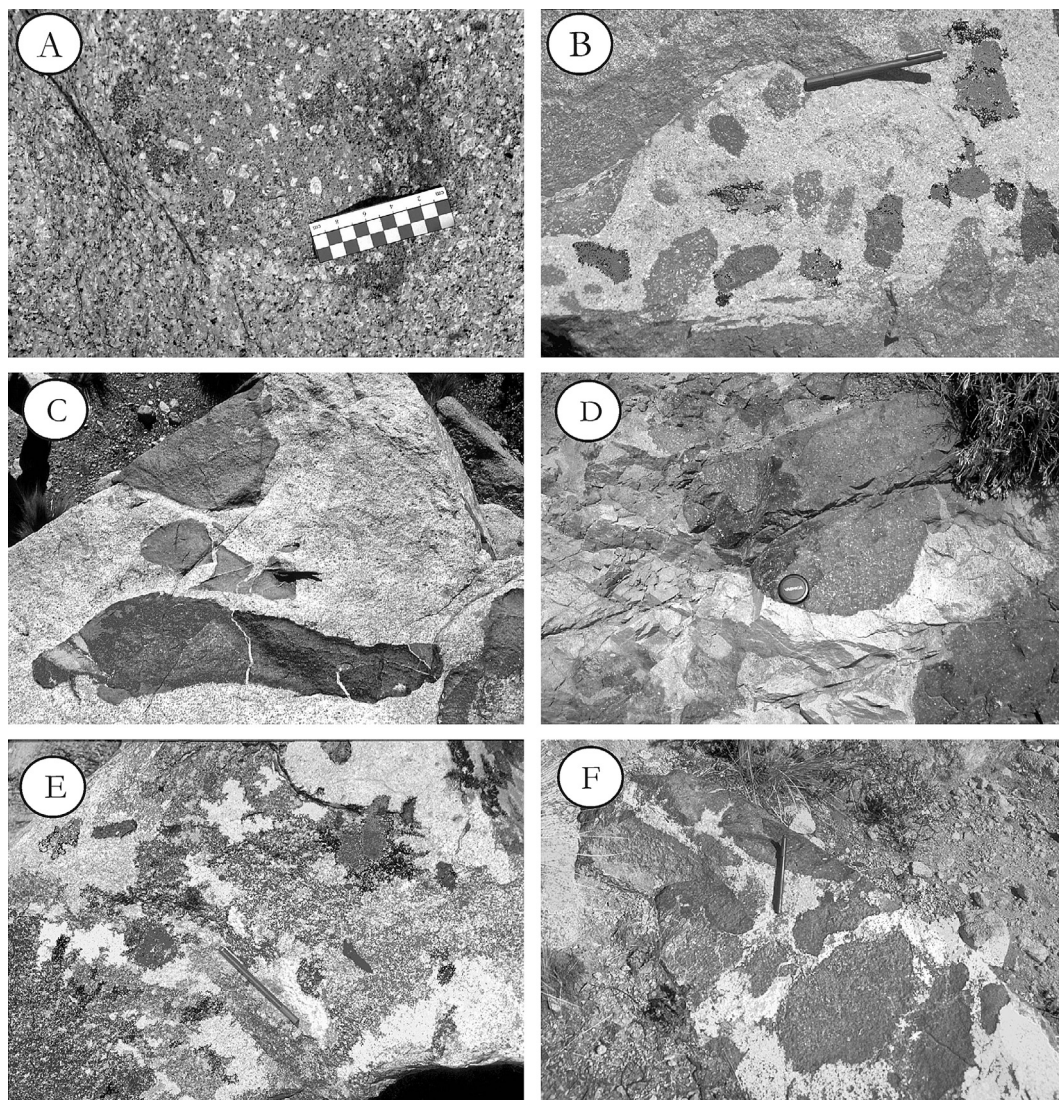
Fig. 3. Photographs illustrating the occurrences of mafic microgranular enclaves in the Aguilar monzogranite. A: Ghosts of medium-grained diorite enclaves within the biotite-hornblende monzogranite. These relationships provide evidence of extensive mingling and partial hybridization between magmas with different composition, during the emplacement of the Aguilar monzogranite. B: Enclaves of fine-grained diorite hosted in syenite (pen = 14 cm). C: Enclaves of fine-grained layered gabbroid rock, showing the sharp contact with the syenite sill-like intrusion. D: Irregular and scalloped contact between syenite intrusion and monzodiorite enclaves (lens cap = 5 cm). E: Example of mingling between mafic and felsic components showing evidence of dismembering of the mafic enclaves, producing locally an intensely hybridized zone (pen = 14 cm). F: Example of mingling between dismembered fine-grained diorite enclaves and the surrounding monzogranite host rock (pen = 14 cm).

ilmenite, apatite, zircon, allanite, and titanite as accessory minerals. Hornblende is absent and biotite is the main mafic mineral along the western side of the pluton and in two irregular masses, one in the northern and another in the southern sectors of the pluton (Fig. 2). Somewhere, the monzogranite shows a porphyritic texture with feldspar megacrysts showing plagioclase cores and K-feldspar rims, yielding a typical anti-rapakivi texture (Vance, 1965; Wark and Stimac, 1992). According to the crystals morphologies and the relations between the two feldspars, two types may be distinguished, 1) plagioclase crystal mantled by K-feldspar, and 2) plagioclase core followed by dendritic plagioclase and successively mantled by K-feldspar ("E" and "F", types respectively; after Hibbard, 1981; Słaby and Götze, 2004).

Quartz-monzonite rocks occur as enclaves and sill-like intrusions in the biotite-hornblende monzogranite. They show porphyritic texture and contain orthoclase, plagioclase, quartz, and biotite as main mineral phases, sometimes with subordinate hornblende. Apatite, titanite, zircon and opaque minerals are the main accessory phases. The quartz-syenite rocks occur as enclaves and sill-like intrusions showing relatively high amount of orthoclase, scarce quartz, and abundant clusters of hornblende and biotite that confer to the rock a high colour index.

3.2. Gabbroid rocks

The gabbroid rocks include some massive bodies and many enclaves dispersed in the biotite-hornblende monzogranite. The enclaves are commonly dark in colour, ellipsoidal to rounded and flattened in shape with the maximum dimension between 5 and 100 cm (Fig. 3). Crystals from host rocks may occur within the enclaves.

The gabbroid rocks, with monzodiorite, quartz-monzodiorite, diorite and gabbro modal composition, show fine to medium-grained, hypidiomorphic texture. Clinopyroxene is an ubiquitous mineral of the gabbroid bodies and enclaves. The gabbro and diorite enclaves have subophitic textures with clinopyroxene enclosing
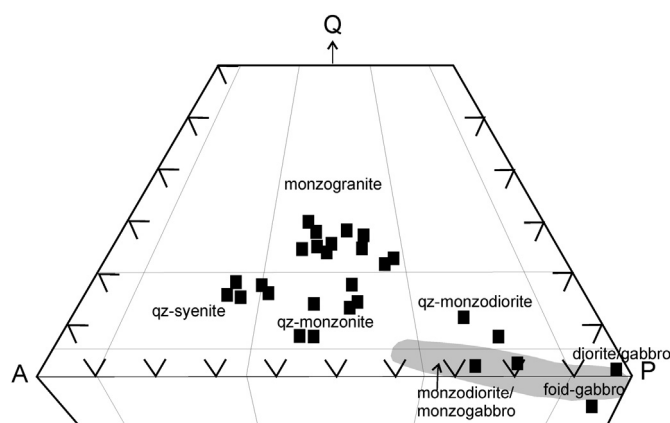
Fig. 4. Modal classification for the rocks from the Aguilar pluton plotted in the QAPF diagram (Streickeisen, 1976). Full square = AG rocks, open square = enclaves. Data source: Cristiani et al. (2005); representative analyses are reported in Table S1.

calcic plagioclase. The plagioclase crystals range in size from 0.5 mm to 1 mm, and show normal and, rarely, oscillatory zoning. The hornblende forms prismatic crystals that enclose cores of clinopyroxene (coronitic texture). Some samples (foid-gabbro) contain low amounts of modal feldspathoids (nepheline?) in a finely-crystallized, interstitial mass.

4. Mineral chemistry

4.1. Feldspars

Plagioclase and alkali feldspar compositions (Table 1) are plotted in Fig. 5A. The plagioclase from gabbroids (e.g. diorite AG31 with $SiO_2 = 47.4$ wt%) exhibits a rather large compositional variation from An_{37-48} (core) to An_{20-21} (rim). On the contrary, the plagioclase from granitoid s.l. rocks with SiO_2 around 60 wt % (AG45ca) shows scarce zoning and oligoclase composition from An_{13-10} (core) to An_{17-7} (rim). The associated alkali feldspar has a composition of Or_{67-94}. The microgranular enclaves (AG45s, with $SiO_2 = 53$ wt%), hosted in the sample AG45ca, show a compositional range from An_{7-14} (core) to An_{11-13} (rim). The monzogranites AG13 ($SiO_2 = 69.4$ wt%) and AG18 ($SiO_2 = 74.0$ wt%) have plagioclase crystals from strongly zoned (core An_{58} to rim An_{12}) to unzoned (e.g. An_{13-11} from core to rim). The associated alkali feldspars have a composition range of Or_{95-94}. The plagioclase crystal analyzed from the sample AG18 gave an average value from An_{13} (core) to An_{11} (rim). The coexisting alkali feldspar shows a compositional range of Or_{74-97} and forms microlites in the groundmass, graphic intergrowth with quartz, or mantling of plagioclase crystals (anti-rapakivi texture).

4.2. Clinopyroxene

Clinopyroxene is a main constituent of the gabbroid bodies and enclaves. It forms large euhedral to subhedral green phenocrysts or glomerocrystals, ca. 4 mm in size, showing variable degrees of alteration with rims of secondary amphiboles. Therefore, it has been analyzed only in the sample which shows the most preserved crystals (AG31; Table 2). In the groundmass, optically unzoned clinopyroxene grains are present (<1 mm). The analyzed crystals have a small compositional range (Fig. 5B) in the diopside field according to the classification of Morimoto (1988). Some normal zoning with Mg# = 0.73−0.70 in the cores and Mg# = 0.70−0.62 in the rims has been observed. Also the Na_2O content increases from

the cores (0.57−0.73 wt%) to the rims (0.82−0.95 wt %). Some crystals show modest reverse zoning (i.e. crystal C3) with Mg# from 0.72 (core) to 0.74 (rim). The Al^{IV} content is low, ranging from 0.15 to 0.19 (core) and 0.15−0.04 (rim) a.f.u. (atoms by formula units).

4.3. Amphibole

Representative amphibole analyses for the main AG rock types are listed in Table 3. The chemistry corresponds to calcic amphiboles according to Leake et al. (1997), and the compositional range is characterized by a broadly continuous variation from hastingsite to ferroedenite, up to ferrohornblende varieties (Table 3 and Fig. 5C). Hastingsite is the amphibole variety in the diorite (AG31; $SiO_2 = 47.49$ wt%) and shows a range of Mg# from 0.39 to 0.46 (Fig. 5C). The total Al contents range from 2.17 to 2.24 a.f.u while the Al^{IV} and Ti are in the range 1.66−2.04 and 0.23−0.40 a.f.u., respectively. The composition of amphibole in the monzodiorite enclaves (AG45s; $SiO_2 = 53.54$ wt%) plots mainly in the hornblende field, while ferroedenite is the dominant amphibole in the monzogranite, with Mg# and Al^{IV} ranging from 0.23 to 0.25 and from 1.2 to 1.49 a.f.u., respectively. The contents of Al_2O_3 and TiO_2 in the amphibole crystals decrease with increasing differentiation grade of the host rock. The amphibole crystals in the diorite AG31 have higher Al_2O_3 (10.21−12.36 wt%) and TiO_2 (2.25−3.46 wt%) in respect to those in the silicic suite (e.g. AG18, $Al_2O_3 = 7.10−8.00$ and $TiO_2 = 0.25−1.77$ wt%) (Table 3).

4.4. Biotite

Representative analyses of biotite composition are listed in Table 4. The biotite has a restricted range of composition in all rock types and plots along the phlogopite-annite tie-line (Fig. 5D). The most Mg-rich biotite compositions are present in the enclave AG45s ($SiO_2 = 53.54$ wt%) with Mg# = 0.36−0.34, $Al^{IV} = 2.34−2.38$ a.f.u. and $TiO_2 = 4.03−4.34$ wt %. In the hornblende-biotite monzogranite (sample AG18; $SiO_2 = 74.04$ wt %), biotite crystals have Mg# = 0.25−0.22, $Al^{IV} = 2.37−2.55$ a.f.u. and $TiO_2 = 3.08−3.58$ wt %. The fluorine plus chlorine contents in biotite are higher in the monzogranite rocks, with a range from 0.90 to 1.26 wt% (core) to 0.72−1.41 wt% (rim), than in the basic rocks, ranging from 0.83 (core) to 0.78 wt% (rim). This tendency is in agreement with F−Cl increase with magmatic differentiation.

5. Geochemistry

The AG rocks show a large variation in SiO_2 content, ranging from 44.8 wt% to 76.6 wt%, and largely plot in the alkaline field, straddling the Irvine and Baragar (1971) line with the most silicic terms (Fig. 6A). In the Na_2O vs. K_2O diagram (inset in Fig. 6A), the AG rocks mainly plot in the potassic and transitional fields, but a few samples fall in the sodic field. The AG rocks are mainly metaluminous, with some samples weakly peraluminous and a few ones close to peralkaline (Fig. 6B). The granitoid rocks have characteristics of A-type granites (Bonin, 2007, and references therein) or "ferroan granites", according to Frost and Frost (2011), having high FeO_t/MgO ratios (Fig. 6C and D).

Variation diagrams for selected major and trace elements plotted against SiO_2 content (Fig. S1) show that the concentration of K_2O increases strongly with the magma evolution. The Al_2O_3 content increases in the SiO_2 interval between 44 and 60 wt% and, then, sharply decreases with further differentiation. Na_2O does not show any significant correlation with SiO_2. In contrast, FeO_t, TiO_2, CaO, MgO, MnO and P_2O_5 show negative trends with increasing SiO_2. Among the trace elements compatible in ferromagnesian

Table 1

Representative feldspar analyses from AG granite (wt %). Structural formula recalculated on the basis of 8 oxygen. C1 = crystal; c = core; i = intermediate zone; r = rim. Microprobe analysis with JEOL JXA-8600-A4 at IGG-CNR, Florence, Italy.

Sample	AG45s	AG45s	AG45s	AG45s	AG45s	AG45s	AG45s	AG45s	AG45ca	AG45ca	AG45ca	AG45ca	AG45ca	AG45ca
	C1c	C1i	C1r	C2c	C2r	C3c	C3r	C4	C1c	C1r	C2c	C2r	C3	C4
SiO_2	66.25	66.00	65.18	64.8	64.73	62.56	66.24	65.27	65.02	66.52	66.16	63.53	65.72	66.54
Al_2O_3	21.61	21.35	21.95	21.62	21.75	25.58	22.17	19.09	22.23	21.83	21.92	23.02	18.66	19.69
FeO	0.14	0.14	0.15	0.11	0.16	0.2	0.07	0.17	0.12	0.1	0.04	0.1	0.16	0.09
CaO	1.98	2.00	2.93	3.09	2.77	1.39	2.32	0.05	2.84	1.38	2.15	3.63	0.05	0.26
Na_2O	10.07	10.37	10.28	10.17	9.56	7.5	9.55	1.43	10.14	9.32	9.7	9.04	0.56	2.83
K_2O	0.35	0.21	0.14	0.17	0.13	2.62	0.18	14.36	0.17	0.21	0.26	0.22	15.17	9.6
Sum	100.4	100.07	100.63	99.96	99.1	99.85	100.53	100.37	100.52	99.36	100.23	99.54	100.32	99.01
Si	2.9	2.9	2.86	2.86	2.87	2.77	2.89	2.98	2.85	2.92	2.89	2.81	3.01	3.01
Al	1.11	1.11	1.13	1.13	1.14	1.33	1.14	1.03	1.15	1.13	1.13	1.2	1.01	1.05
Fe	0.01	0.01	0.01	0	0.01	0.01	0	0.01	0	0	0	0	0.01	0
Ca	0.09	0.09	0.14	0.15	0.13	0.07	0.11	0	0.13	0.06	0.1	0.17	0	0.01
Na	0.85	0.88	0.87	0.87	0.82	0.64	0.81	0.13	0.86	0.79	0.82	0.78	0.05	0.25
K	0.02	0.01	0.01	0.01	0.01	0.15	0.01	0.84	0.01	0.01	0.01	0.01	0.89	0.55
An	9.60	9.52	13.5	14.24	13.7	7.69	11.71	0.25	13.28	7.46	10.74	17.93	0.26	1.55
Ab	88.38	89.29	85.73	84.82	85.54	75.06	81.21	13.11	85.78	91.19	87.71	80.78	5.3	30.46
Or	2.02	1.19	0.77	0.93	0.77	17.25	1.08	86.63	0.95	1.35	1.55	1.29	94.44	67.99

Sample	AG18	AG18	AG18	AG18	AG18	AG18	AG18	AG18	AG18	AG18	AG18	AG18	AG18	AG18
	C1c	C1r	C2c	C2r	C3c	C3r	C4c	C4r	C5c	C5r	C6	C7	C8	C9	C10
SiO_2	67.86	66.42	65.2	64.94	65.27	65.33	65.01	66.65	65.13	65.44	63.86	63.67	64.08	64.23	65.75
Al_2O_3	21.57	22.23	22.99	21.81	22.36	22.36	22.96	21.55	22.25	21.98	19.54	19.58	19.44	19.76	19.77
FeO	0.05	0.21	0.14	0.06	0.16	0.13	0.12	0.13	0.15	0.13	0.18	0.14	0.03	0.13	0.07
CaO	0.55	2.03	2.35	2.13	2.65	2.20	3.16	2.34	2.47	2.27	0.06	0.05	0.04	0.08	0.05
Na_2O	9.56	8.24	8.87	10.38	10.1	9.66	9.35	9.99	9.3	10.02	0.24	0.29	0.17	0.58	2.8
K_2O	0.11	0.53	0.13	0.17	0.29	0.66	0.38	0.31	0.26	0.29	15.13	15.27	15.92	15.11	12.26
Sum	99.7	99.66	99.68	99.49	100.83	100.34	100.98	100.97	99.56	100.13	99.01	99.00	99.68	99.89	100.7
Si	2.95	2.91	2.86	2.87	2.85	2.86	2.84	2.9	2.87	2.87	2.96	2.96	2.96	2.96	2.97
Al	1.11	1.15	1.19	1.14	1.15	1.16	1.18	1.11	1.16	1.14	1.07	1.07	1.06	1.07	1.05
Fe	0	0.01	0.01	0	0.01	0	0	0	0.01	0	0.01	0.01	0	0.01	0
Ca	0.03	0.1	0.11	0.1	0.12	0.1	0.15	0.11	0.12	0.11	0	0	0	0	0
Na	0.81	0.7	0.75	0.89	0.86	0.82	0.79	0.84	0.79	0.85	0.02	0.03	0.02	0.05	0.25
K	0.01	0.03	0.01	0.01	0.02	0.04	0.02	0.02	0.01	0.02	0.9	0.91	0.94	0.89	0.71
An	3.06	11.55	12.66	10.09	12.46	10.75	15.39	11.26	12.6	10.94	0.32	0.27	0.21	0.42	0.25
Ab	96.21	84.86	86.5	88.95	85.92	85.41	82.41	86.97	85.83	87.39	2.35	2.8	1.59	5.49	25.7
Or	0.73	3.59	0.83	0.96	1.62	3.84	2.2	1.78	1.58	1.66	97.33	96.94	98.2	94.09	74.04

Sample	AG 13	AG 13	AG 13	AG 13	AG 13	AG 13	AG 13	AG 13	AG31	AG31	AG31	AG31	AG31	AG31
	C1c	C1r	C2c	C2r	C3	C4	C5	C6	C1	C2	C3c	C3r	C4c	C4r
SiO_2	64.75	65.5	53.52	65.75	64.11	62.75	65.44	64.59	61.43	60.56	53.94	61.88	57.94	62.69
Al_2O_3	22.12	22.18	30.14	21.88	22.97	23.98	18.87	18.74	24.55	24.48	28.68	24.54	26.99	24.15
FeO	0.14	0.05	0.14	0.16	0.2	0.08	0.1	0.1	0.11	0.2	0.22	0.19	0.09	0.11
CaO	2.41	2.77	12.16	2.49	2.73	4.82	0.04	0.01	5.4	5.51	10.29	4.46	7.24	4.03
Na_2O	9.61	10.03	4.64	9.67	8.91	8.33	0.49	0.63	8.2	8.4	5.96	8.88	6.67	8.62
K_2O	0.22	0.34	0.22	0.19	0.33	0.24	15.85	16.65	0.34	0.31	0.09	0.18	0.1	0.12
Sum	99.25	100.87	100.82	100.14	99.2	100.2	100.79	100.72	100.03	99.46	99.18	100.13	99.03	99.72
Si	2.87	2.86	2.4	2.88	2.84	2.77	2.99	2.98	2.73	2.71	2.46	2.74	2.60·	2.77
Al	1.15	1.14	1.6	1.13	1.2	1.25	1.02	1.02	1.28	1.29	1.54	1.28	1.43	1.26
Fe	0.01	0.00	0.01	0.01	0.01	0.00	0.00	0.00	0.00	0.01	0.01	0.01	0.00	0.00
Ca	0.11	0.13	0.59	0.12	0.13	0.23	0	0	0.26	0.26	0.5	0.21	0.35	0.19
Na	0.82	0.85	0.4	0.82	0.76	0.71	0.04	0.06	0.71	0.73	0.53	0.76	0.58	0.74
K	0.01	0.02	0.01	0.01	0.02	0.01	0.92	0.98	0.02	0.02	0.01	0.01	0.01	0.01
An	12.01	12.99	58.41	12.32	14.18	23.89	0.20	0.05	26.16	26.14	48.58	21.5	37.26	20.38
Ab	86.68	85.11	40.33	86.56	83.77	74.7	4.48	5.44	71.88	72.11	50.92	77.47	62.12	78.89
Or	1.31	1.90	1.26	1.12	2.04	1.42	95.32	94.52	1.96	1.75	0.51	1.03	0.61	0.72

minerals, Ni and Cr for the most primitive samples are dispersed in the diagram against SiO_2, whereas V and Co show a regular decreasing trend with increasing SiO_2. Although scattered, Y defines a poor bell-shaped correlation with SiO_2, while Zr exhibits a well-defined bell-shaped trend. Rb shows scattered points for low silica contents and an increase with silica after 55 wt%. The Sr contents show a negative correlation with SiO_2 in the felsic rocks, and strong scattering in the less differentiated samples. In general, several major and trace elements plotted vs. silica show scattered values in the mafic samples, an inflection in the trend at 55–60 wt% SiO_2, and a regular trend above 60 wt% SiO_2.

The rare earth element patterns and the trace elements spider-diagrams are reported in Fig. 7 for the granitoid (Fig. 7A, B) and gabbroid (Fig. 7C, D) rocks. The granitoid rocks are compared to the muscovite-bearing peraluminous Tusaquillas granite, representing the crustal magma of the plutonic suite (Cristiani et al., 2005). The gabbroid rocks are compared to the Castro Tolay sample T6 (Cristiani et al., 2005), representing the most primitive mafic rock in the
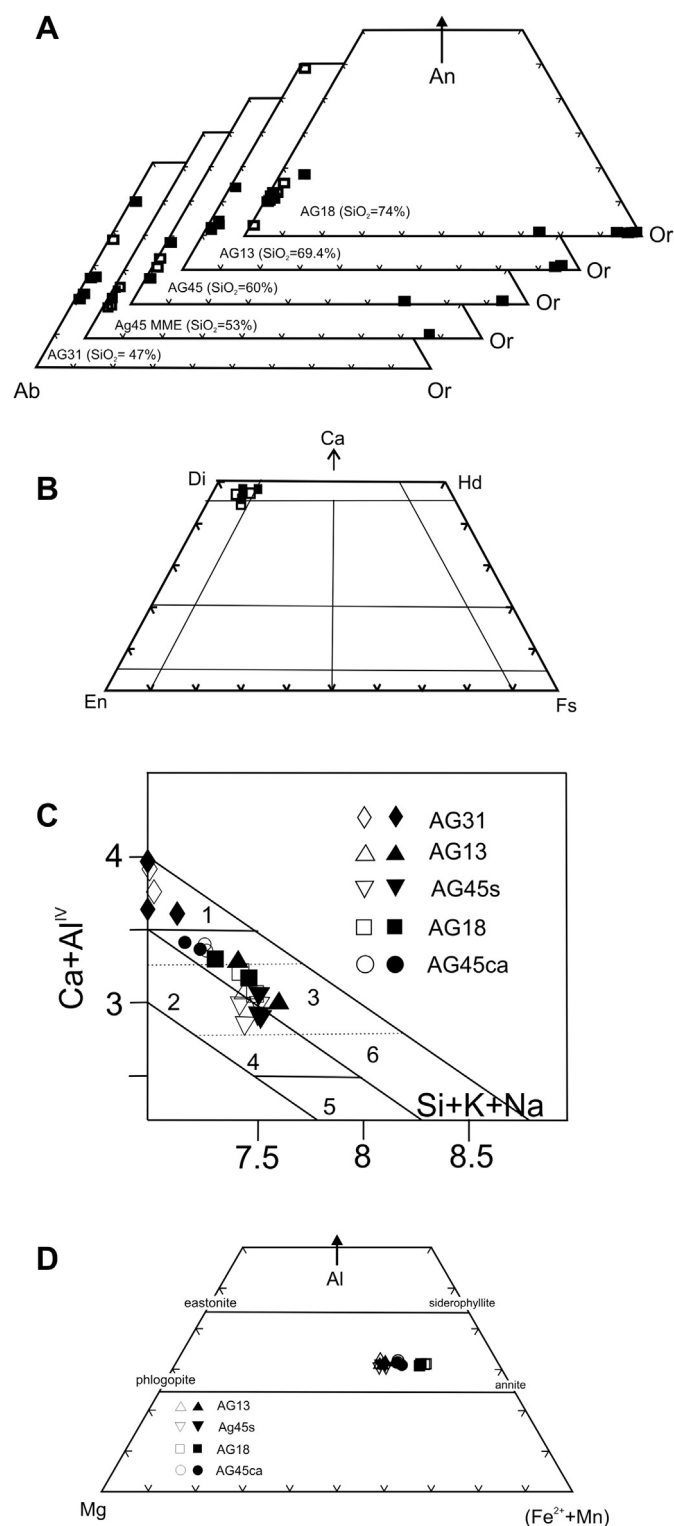
Fig. 5. Mineral composition from selected samples representative of the Aguilar pluton rock types: A) Feldspar composition, plotted into Or-Ab-An (mol%) diagram. Open and full symbols are cores and rims, respectively. B) Clinopyroxene compositions, symbols as in Fig. 5A. Classification diagram after Morimoto (1988). C) Amphibole composition plotted in Ca + Al^{IV} vs Al + K + Na diagram after Giret et al. (1980); (1) hastingsite; (2) hornblende; (3–6) edenite; (4) actinolitic hornblende; (5) actinolite. D: Biotite composition plotted in the Al–Mg–(Fe^{+2} + Mn) diagram (cf. Bailey, 1984 and references therein).

Table 2

Representative pyroxene analyses from Aguilar granite (wt %). Structural formula recalculated on the basis of 6 oxygens. C1 = crystal; c = core; r = rim; bdl: below detection limit. Analytical techniques: see Table 1.

Sample	AG31	AG31	AG31	AG31	AG31	AG31
	C1c	C1r	C2c	C2r	C3c	C3r
SiO$_2$	51.05	50.03	48.95	48.20	49.03	53.05
TiO$_2$	0.76	1.15	1.2	2.08	1.45	0.13
Al$_2$O$_3$	3.99	3.90	6.75	5.33	6.35	0.66
FeO	5.70	6.30	5.72	7.62	5.45	5.31
MnO	bdl	bdl	bdl	bdl	bdl	bdl
MgO	15.80	14.75	13.86	12.90	14.45	15.43
CaO	22.13	22.92	22.79	23.2	22.54	24.98
Na$_2$O	0.57	0.95	0.73	0.82	0.73	0.44
Cr$_2$O$_3$	bdl	bdl	bdl	bdl	bdl	bdl
Sum	100	100	100	100	100	100
Si	1.86	1.82	1.77	1.76	1.78	1.9
Ti	0.02	0.03	0.03	0.05	0.05	0.00
Al^{IV}	0.15	0.15	0.18	0.2	0.19	0.04
Sum	2.03	2.00	1.98	2.01	2.02	1.94
Al^{VI}	0.05	0.01	0.08	0.02	0.07	0.00
Fe^{3+}	0.08	0.16	0.11	0.13	0.09	0.1
Fe^{2+}	0.11	0.05	0.08	0.11	0.05	0.08
Mg	0.87	0.85	0.78	0.75	0.82	0.89
Ca	0.88	0.91	0.9	0.93	0.88	1.01
Na	0.05	0.07	0.04	0.07	0.04	0.04
Sum	2.04	2.05	1.99	2.01	1.95	2.12
Wo	45.62	47.52	49.01	49.3	48.32	49.73
En	45.16	42.32	41.54	39.7	42.62	42.12
Fs	9.22	10.16	9.45	11.1	9.06	8.15
Mg/(Mg + Fe^{2+})	0.73	0.70	0.70	0.64	0.72	0.74

plutonic suite. The AG granitoids show higher LREE, higher La/Yb and minor Eu negative anomaly in respect to the Tusaquillas granitoid, and evident Ba, Sr, P and Ti troughs. With regard to the mafic rocks, they show higher REE content, both light and heavy, than the Castro Tolay sample, and higher content in both LILE and HFSE.

In the AG rocks, the range of initial ^{87}Sr/^{86}Sr is 0.703198–0.704605, calculated at 149 Ma (Cristiani et al., 2005) (see Supplementary Files). This is a modest variation compared to the large variation in SiO$_2$ content from 45.3 to 69.4 wt%. As regards the Nd isotopic ratios, (^{143}Nd/^{144}Nd)$_t$ values range from 0.512392 to 0.512642, calculated at 149 Ma, corresponding to a range in ε^{t}Nd from −1.06 to 3.82 (Fig. 8).

6. Discussion

6.1. The Aguilar pluton

6.1.1. Magma sources

The rocks forming the AG pluton represent a nearly continuous suite from gabbroid to granitoid compositions. For discussing the origin of the AG rocks, we compare them with the most silicic granitoids and the most primitive rocks of the Late Jurassic-Early Cretaceous magmatism in NW Argentina. The AG granitoids do not correspond, in their mineralogical and geochemical composition, to the muscovite-bearing peraluminous Tusaquillas granite (Fig. 7A, B). Instead, the low Sr and high Nd isotopic ratios of the entire AG suite and the continuous trends observed in most major and trace elements geochemical diagrams suggest that differentiation of mantle-derived magmas was a major process in the genesis of the AG rocks.

Some constraints on the nature of the mantle source can be obtained from the mafic AG rocks. However, none of the AG rocks represent unmodified mantle-derived magma, although some show relatively high MgO, Ni, Cr and V contents as well as low

Table 3
Representative amphibole analyses from Aguilar granite. Structural formula on the basis of 23 oxygens. c, core; r, rim; bdl: below detection limit. Analytical techniques: see Table 1.

Sample	AG13	AG13	AG13	AG18	AG18	AG18	AG18	AG31	AG31	AG31	AG31	AG31
	C1c	C2c	C2r	C3c	C3r	C4c	C4r	C5c	C5r	C6c	C6r	C7c
SiO_2	44.18	44.26	43.63	41.76	41.50	0.25	41.94	40.77	38.78	41.44	39.87	38.91
TiO_2	1.43	1.30	1.66	1.20	1.30	0.25	1.77	2.25	3.10	2.04	3.04	3.46
Al_2O_3	8.95	6.63	7.43	8.10	7.69	8.00	7.10	11.97	12.31	10.21	11.66	12.36
FeO	17.97	22.57	22.94	28.5	28.81	29.22	28.97	21.84	20.89	20.38	20.8	21.15
MnO	0.51	0.74	0.68	0.78	0.77	0.70	0.74	0.47	0.41	0.55	0.50	0.48
MgO	9.98	7.45	7.04	4.22	4.13	4.17	3.96	7.46	7.03	8.32	7.21	7.15
CaO	11.91	10.99	10.97	10.14	10.46	10.61	10.23	10.99	11.57	11.81	11.46	11.53
Na_2O	1.89	1.81	1.68	2.20	2.09	2.09	2.18	2.07	2.45	1.92	2.12	2.41
K_2O	1.09	0.84	0.92	1.26	1.18	1.14	1.00	1.24	1.23	1.06	1.24	1.26
F	0.00	0.35	0.15	0.80	0.80	0.83	0.73	0.15	0.00	0.21	0.31	0.18
Cl	0.00	0.21	0.24	0.22	0.28	0.25	0.33	0.28	0.22	0.21	0.18	0.12
Cr_2O_3	0.30	bdl	bdl	0.02	bdl	bdl	bdl	bdl	0.04	bdl	bdl	bdl
Sum	98.21	97.15	97.34	99.2	99.01	98.91	98.95	99.49	98.03	98.15	98.39	99.01
Si	6.65	6.88	6.76	6.54	6.54	6.43	6.62	6.14	6.01	6.34	6.14	5.96
Al^{iv}	1.35	1.12	1.24	1.46	1.43	1.49	1.32	1.86	1.99	1.66	1.86	2.04
Sum	8.00	8.00	8.00	8.00	7.97	7.92	7.94	8.00	8.00	8.00	8.00	8.00
Al^{vi}	0.24	0.09	0.12	0.03	0.00	0.00	0.00	0.26	0.25	0.19	0.25	0.19
Ti	0.16	0.15	0.19	0.14	0.15	0.14	0.21	0.25	0.36	0.23	0.35	0.4
Cr	0.04	0.00	0.00	0.00	0.00	0.00	0.00	0.00	0.00	0.00	0.00	0.00
Fe^{3+}	0.15	0.36	0.40	0.82	0.76	0.90	0.70	0.70	0.20	0.35	0.25	0.30
Fe^{2+}	2.11	2.58	2.57	2.92	3.04	2.96	3.12	2.05	2.51	2.26	2.42	2.41
Mn	0.07	0.10	0.09	0.10	0.10	0.09	0.10	0.06	0.05	0.07	0.07	0.06
Mg	1.24	1.73	1.63	0.99	0.97	0.98	0.93	1.67	1.62	1.9	1.65	1.63
Ca	1.92	1.83	1.82	1.70	1.77	1.80	1.73	1.77	1.92	1.94	1.89	1.89
Na	0.55	0.55	0.50	0.67	0.64	0.64	0.67	0.60	0.74	0.57	0.63	0.72
K	0.21	0.17	0.18	0.25	0.24	0.23	0.20	0.24	0.24	0.21	0.24	0.25
Sum	7.69	7.55	7.50	7.62	7.67	7.74	7.66	7.60	7.89	7.72	7.75	7.85
$Mg/Mg + Fe^2$	0.42	0.40	0.39	0.25	0.24	0.25	0.23	0.45	0.39	0.46	0.41	0.40

Sample	AG45ca	AG45ca	AG45ca	AG45ca	AG45s	AG45s	AG45s	AG45s	AG45s	AG45s
	C8c	C8r	C9c	C9r	C10c	C10r	C11c	C11r	C12c	C12r
SiO_2	46.1	45.67	45.67	46.41	44.56	43.26	43.49	43.44	42.93	44.1
TiO_2	1.18	1.59	1.21	1.25	1.71	1.93	1.91	1.77	2.02	1.83
Al_2O_3	5.47	5.60	5.74	5.60	6.75	7.15	7.15	6.85	7.29	7.05
FeO	22.72	21.77	22.57	22.74	24.21	24.00	24.16	24.41	25.07	24.65
MnO	0.70	0.63	0.53	0.66	0.61	0.74	0.72	0.73	0.77	0.69
MgO	8.10	8.08	8.25	8.09	6.96	6.72	6.71	6.78	5.90	6.48
CaO	11.00	11.26	11.35	11.11	10.28	10.19	10.13	10.22	10.31	9.95
Na_2O	1.40	1.54	1.09	1.46	1.80	1.82	2.08	1.91	2.12	2.03
K_2O	0.63	0.65	0.64	0.63	0.78	0.83	0.88	0.78	0.90	0.76
F	0.20	0.31	0.26	0.41	bdl	0.30	bdl	0.31	bdl	0.41
Cl	0.14	0.13	0.12	0.17	bdl	0.25	bdl	0.28	bdl	0.31
Cr_2O_3	0.01	0.01	0.02	0.01	0.05	bdl	bdl	bdl	bdl	0.02
Sum	97.65	97.24	97.45	98.54	97.71	97.19	97.23	97.48	97.31	98.28
Si	7.04	7.05	7.02	7.05	6.82	6.71	6.72	6.72	6.69	6.77
Al^{iv}	0.96	0.95	0.98	0.95	1.18	1.29	1.28	1.25	1.31	1.23
Sum	8.00	8.00	8.00	8.00	8.00	8.00	8.00	7.97	8.00	8.00
Al^{vi}	0.03	0.07	0.05	0.05	0.03	0.01	0.02	0.00	0.03	0.05
Ti	0.14	0.18	0.14	0.14	0.20	0.23	0.22	0.21	0.24	0.21
Cr	0.00	0.00	0.00	0.00	0.01	0.00	0.00	0.00	0.00	0.00
Fe^{3+}	0.52	0.21	0.51	0.45	0.69	0.73	0.67	0.77	0.55	0.73
Fe^{2+}	2.38	2.60	2.37	2.44	2.40	2.38	2.45	2.39	2.71	2.44
Mn	0.09	0.08	0.07	0.08	0.08	0.10	0.09	0.10	0.10	0.09
Mg	1.84	1.86	1.87	1.83	1.59	1.55	1.54	1.56	1.37	1.48
Ca	1.80	1.86	1.85	1.81	1.68	1.69	1.68	1.69	1.72	1.64
Na	0.41	0.46	0.32	0.43	0.53	0.55	0.62	0.57	0.64	0.60
K	0.12	0.13	0.12	0.12	0.15	0.16	0.17	0.15	0.18	0.15
Sum	7.33	7.45	7.30	7.35	7.36	7.40	7.46	7.44	7.54	7.39
$Mg/Mg + Fe^2$	0.44	0.42	0.44	0.43	0.40	0.40	0.39	0.40	0.34	0.38

$(^{87}Sr/^{86}Sr)_i$ and high $(^{143}Nd/^{144}Nd)_i$ suggesting scarce modification by fractional crystallization or crustal contamination processes. Among these, both slightly silica-undersaturated and saturated rocks are found, but the strong analogy in the trace element patterns (Fig. 7C–D), as well as the equivalent mineralogical composition (Fig. 5), suggests that AG silica undersaturated and saturated mafic rocks derive from a similar mantle source.

The AG pluton mafic rocks are compared to the Castro Tolay gabbros (154 Ma, sample T6 in Figs. 7 and 8; Cristiani et al., 2005) and the Rio Grande lamprophyres (163 Ma, sample P8 and field RG in Fig. 8, Hauser et al., 2010). As regards the isotopic composition, the AG mafic samples show a close correspondence with the Castro Tolay gabbro (Fig. 8). In general, the rocks of the AG pluton fall within the Sr and Nd isotope range for the peridotite xenoliths

Table 4

Representative biotite analyses from Aguilar granite. Structural formula recalculated on the basis of 22oxygens. C1 = crystal; c = core; r = rim; bdl: below detection limit. Analytical techniques: see Table 1.

Sample	AG45s	AG45s	AG45s	AG45s	AG45ca	AG45ca	AG45ca	AG45ca
	C1c	C1r	C2c	C3c	C1c	C1r	C2c	C2r
SiO_2 (wt%)	36.06	36.45	36.16	35.96	35.37	35.49	35.18	35.42
TiO_2	4.34	4.22	4.21	4.03	4.17	3.29	4.02	4.05
Al_2O_3	12.78	12.89	12.75	12.82	12.79	13.04	12.51	13.06
FeO	25.03	24.85	25.44	25.52	26.52	26.83	26.98	26.45
MnO	0.34	0.27	0.31	0.37	0.24	0.34	0.26	0.26
MgO	8.23	P0.27	7.91	7.84	6.88	6.91	6.58	6.7
CaO	0.06	0.04	0.11	0.03	0.08	0.02	0.04	0.04
Na_2O	bdl	0.16	0.08	0.10	0.04	0.04	0.10	0.02
K_2O	9.76	9.69	9.51	9.59	9.42	9.11	9.3	8.95
Cr_2O_3	0.05	bdl	bdl	bdl	0.01	bdl	bdl	0.06
F	0.61	0.55	0.46	0.43	0.41	bdl	0.31	0.26
Cl	0.22	0.23	0.24	0.26	0.25	bdl	0.23	0.23
Sum	97.48	97.62	97.18	96.95	96.18	95.07	95.51	95.5
Si	5.62	5.66	5.65	5.64	5.62	5.66	5.64	5.64
Al^{IV}	2.35	2.34	2.35	2.36	2.38	2.34	2.36	2.36
Ti	0.03	0.00	0.00	0.00	0.00	0.00	0.00	0.00
Sum	8.00	8.00	8.00	8.00	8.00	8.00	8.00	8.00
Al^{VI}	0.00	0.01	0.00	0.01	0.02	0.11	0.00	0.09
Ti	0.48	0.49	0.49	0.48	0.50	0.39	0.48	0.48
Fe^{2+}	3.27	3.23	3.33	3.35	3.53	3.58	3.62	3.52
Mn	0.04	0.04	0.04	0.05	0.03	0.05	0.04	0.04
Mg	1.91	1.91	1.84	1.83	1.63	1.64	1.57	1.50
Cr	0.01	0.00	0.00	0.00	0.00	0.00	0.00	0.01
Ca	0.01	0.01	0.02	0.01	0.01	0.00	0.01	0.01
Na	0.00	0.05	0.02	0.03	0.01	0.01	0.03	0.01
K	1.94	1.92	1.90	1.92	1.91	1.85	1.90	1.82
Sum	7.66	7.66	7.64	7.68	7.64	7.63	7.65	7.48
Mg/Mg + Fe + Mn	0.36	0.36	0.35	0.34	0.31	0.31	0.30	0.30
Sample	AG18	AG18	AG18	AG18	AG13	AG13	AG13	AG13
	C1c	C1r	C2c	C2r	C1c	C1r	C2c	C2r
SiO_2 (wt%)	34.66	34.33	34.13	33.81	35.70	36.28	35.33	35.47
TiO_2	3.58	3.54	3.08	3.18	4.27	4.43	4.39	4.02
Al_2O_3	12.56	12.43	12.55	13.01	12.43	13.11	12.79	12.48
FeO	29.67	28.92	31.55	32.74	24.75	24.18	24.84	24.66
MnO	0.36	0.32	0.29	0.28	0.34	0.27	0.32	0.31
MgO	5.04	5.25	5.83	5.36	7.94	7.87	7.61	8.14
CaO	0.13	0.11	0.12	0.11	0.11	0.05	0.02	0.03
Na_2O	bdl	bdl	bdl	0.07	0.08	0.17	0.08	0.10
K_2O	8.82	8.19	8.39	7.35	8.98	9.41	9.41	9.38
Cr_2O_3	0.01	bdl	0.02	0.02	bdl	0.02	bdl	bdl
F	0.89	1.39	0.57	0.44	0.47	0.49	0.57	0.34
Cl	0.37	0.29	0.33	0.28	0.38	0.36	0.36	0.37
Sum	96.09	94.77	96.91	96.65	95.45	96.64	95.72	95.3
Si	5.63	5.65	5.52	5.45	5.67	5.67	5.62	5.65
Al^{IV}	2.37	2.35	2.40	2.47	2.32	2.33	2.38	2.34
Ti	0.00	0.00	0.08	0.08	0.01	0.00	0.00	0.01
Sum	8.00	8.00	8.00	8.00	8.00	8.00	8.00	8.00
Al^{VI}	0.04	0.06	0.00	0.00	0.00	0.08	0.01	0.00
Ti	0.44	0.44	0.37	0.39	0.51	0.52	0.52	0.47
Fe^{2+}	4.04	3.99	4.27	4.42	3.29	3.16	3.31	3.29
Mn	0.05	0.04	0.04	0.04	0.05	0.04	0.04	0.04
Mg	1.22	1.29	1.41	1.29	1.88	1.83	1.8	1.93
Cr	0.00	0.00	0.00	0.06	0.06	0.00	0.00	0.00
Ca	0.02	0.02	0.02	0.02	0.02	0.01	0.00	0.01
Na	0.00	0.00	0.00	0.02	0.02	0.05	0.02	0.03
K	1.83	1.72	1.73	1.51	1.82	1.88	1.91	1.91
Sum	7.64	7.56	7.76	7.67	7.58	7.57	7.61	7.68
Mg/Mg + Fe + Mn	0.22	0.27	0.24	0.22	0.36	0.36	0.34	2.72

reported by Lucassen et al. (2005) and Comin-Chiaramonti et al. (2009) for the Central Andes (Fig. 8). The negative initial ε^tNd values indicate that some crustal contamination is, also, required to generate the final granitoid rocks. As regards the trace elements composition, the AG mafic rocks display a REE enrichment, in respect to the Castro Tolay sample, which could be explained with their higher differentiation degree. Although the isotopic

composition of AG mafic rocks and Castro Tolay sample T6 are close, minor crustal contamination could have contributed to the REE enrichment (Fig. 8). The Rio Grande lamprophyre, instead, shows a remarkably higher La/Yb (74.5 for sample P8), that is indicative of a very low degree of partial melting (Fig. 7C–D). In AG mafic rocks, LREE are moderately fractionated with La/Sm ranging from 5.6 to 6.1 ppm, while La/Yb varies from 14.2 to 17.8 ppm due to the
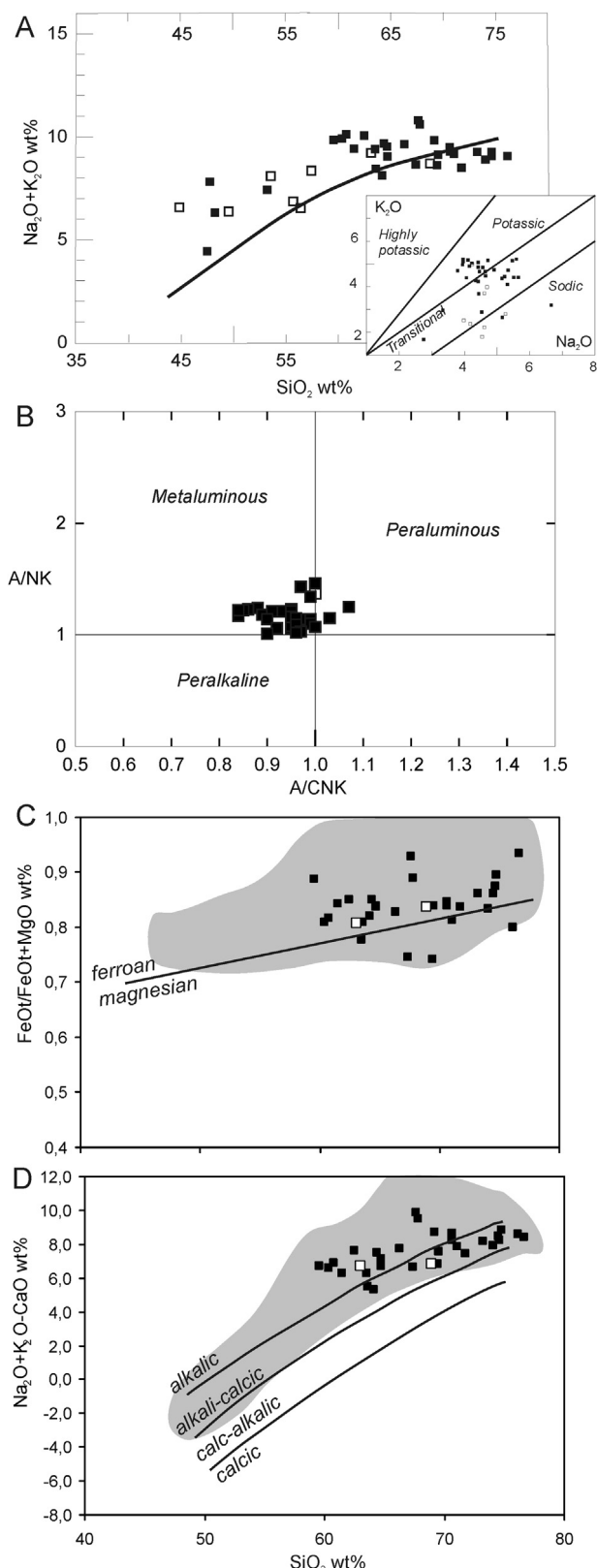
variable HREE content with constant LREE. This suggests that HREE were retained in a residual phase during partial melting of the source, or that fractionation of a HREE-bearing phase occurred. On the other hand, different degrees of partial melting of a same source seem unlikely considering the constant ratios of some trace elements (i.e Nb/Yb values). Since the Sr and Nd isotopic ratios are moderately different, a weak crustal contamination during the mafic magma ascent and early differentiation stages could explain the presence of hy-normative and ne-normative mafic rocks. In particular, the hy-normative sample AG31 shows a significantly higher $^{87}Sr/^{86}Sr$ than the ne-normative gabbroid samples (AG8; Fig. 8).

The nature of the mantle source can be discussed by means of the model of Sm–Nd depleted mantle ages (T_{DM}; DePaolo, 1988). The analyzed samples of the AG pluton display T_{DM} ages between 1.06 and 0.60 Ga, that are quite different in respect to those of the Rio Grande lamprophyres, ranging from 0.64 to 0.25 Ga (Fig. 9). These data suggest that the AG and Rio Grande igneous suites belong to different magma lineages, linked to geochemically distinct mantle reservoirs. Moreover, the initial $^{87}Sr/^{86}Sr$ isotopic ratios and the lower incompatible and REE elements contents of AG rocks, compared with the Rio Grande rocks (see Hauser et al., 2010), preclude the possibility that the AG magmas were generated from the enriched metasomatized lithospheric mantle representing the source of the Rio Grande lamprophyres magmas. Rather, our data suggest that the AG magmas, as well as the Castro Tolay ones, could be derived from a chemically and isotopically uniform mantle resulted from the geodynamic evolution during the Proterozoic. We propose the following geological and geochemical evolution. The mantle source of the AG magmas experienced episodes of depletion compatible with the extraction of tholeiite basalt magmas during the break-up of the Rodinia supercontinent between 0.78 and 0.54 Ga (Omarini et al., 1999). The oldest T_{DM} 1.06 Ga age is consistent with the aggregation, before the Rodinia fragmentation, of the supercontinent's autochthonous basement with ancient protoliths and typical Grenville rocks. On the other hand, the Rio Grande magmas, showing the prominent T_{DM} ages interval from 0.64 to 0.42 Ga, could derive from an upper Precambrian lithospheric mantle source which was metasomatized by subduction processes during Early Cambrian (Tilcarian Orogeny; 0.56–0.52 Ga) and/or Early Ordovician (Famatinian Orogeny; 0.50–0.45 Ga) (Lucassen et al., 2005, 2007; Hauser et al., 2011; Escayola et al., 2011). The youngest Rio Grande T_{DM} age of 0.25 Ga could be related to the magmatic events during the early stage of the Mesozoic ensialic rifting (Sempere et al., 2002).

6.1.2. Petrographic and mineralogical evidence for petrogenetic processes

The presence of core-to-rim zoning in plagioclase (Fig. 5A) and the compositional ranges of amphibole and biotite crystals from gabbroid to granitoid rocks (see Fig. 5C, D and the variation of Mg/Mg + Fe values in Tables 3 and 4), joined to the major and trace elements trends are a compelling evidence for crystal fractionation processes during the magmatic differentiation of the AG pluton suite. Fractional crystallization involved firstly ferromagnesian minerals and negligible plagioclase, as suggested by the behavior of Al_2O_3 and Sr and the lack of Eu anomaly in REE patterns (Fig. 7A, Fig. S1). For a SiO_2 content of magmas >60 wt%, fractional

Fig. 6. A. TAS (total alkalis versus silica, in wt.%, cf. Le Maitre et al., 1989; modified by Middlemost, 1994) for the Aguilar pluton rocks. Black line separates the alkaline and subalkaline fields (after Irvine and Baragar, 1971). Full square = AG rocks, open square = enclaves. Inset: Na_2O vs. K_2O diagram showing the potassic vs. sodic character of the Aguilar rocks and microgranular enclaves. Data source: Cristiani et al. (2005); representative analyses are reported in Table S1. B. Alumina Saturation Index A/CNK (=molar Al_2O_3/[CaO + Na_2O + K_2O]) versus A/NK (=molar Al_2O_3/[Na_2O + K_2O]) for AG granitoid rocks. C and D: geochemical classification of AG granitoid rocks following Frost et al. (2001). The grey fields indicate 486 samples of anorogenic rocks (Frost et al., 2001). The line in C divides the ferroan (above) from the magnesian (below) rock-types; the lines in D divide the alkalic, alkali-calcic, calc-alkalic and calcic rocks (Frost and Frost, 2011). Symbols as in Fig. 6A.
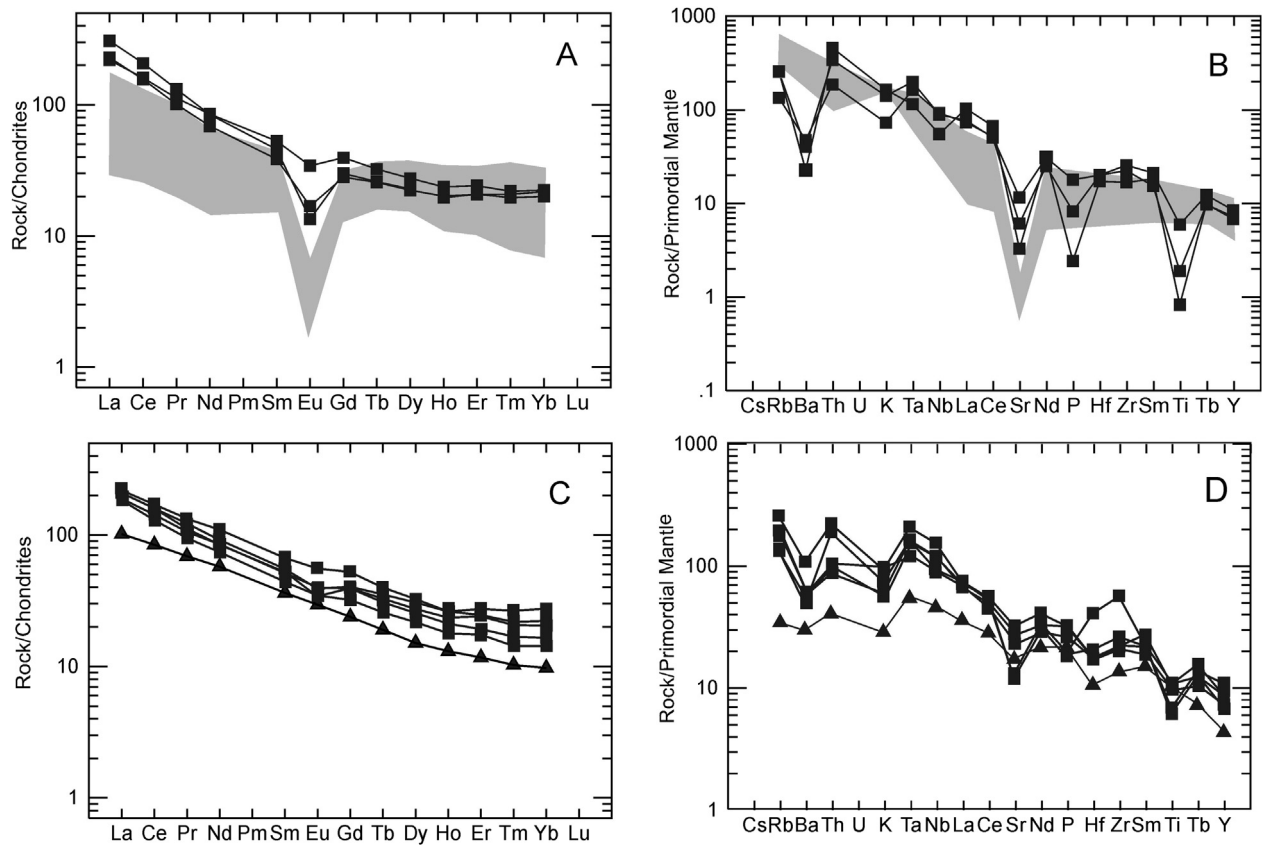
Fig. 7. A. Initial Sr (R_o) and Nd (^{t}Nd) isotopic ratios of AG rocks, calculated at 149 Ma (Cristiani et al., 2005). For comparison, the diagram shows fields for the mantle-derived rocks representative of the old subcontinental mantle from Lucassen et al. (2002, 2005) (light grey), the Rio Grande alkaline lamprophyres (RG field and sample P8, from Hauser et al., 2010), the Castro Tolay gabbro (T6, from Cristiani et al., 2005). MORB and OIB fields after Zindler and Hart (1986). B. Variation of initial ^{87}Sr/^{86}Sr ratios (R_o) against SiO$_2$ for AG rocks; Castro Tolay gabbro T6 and Tusaquillas silicic rocks from Cristiani et al. (2005).
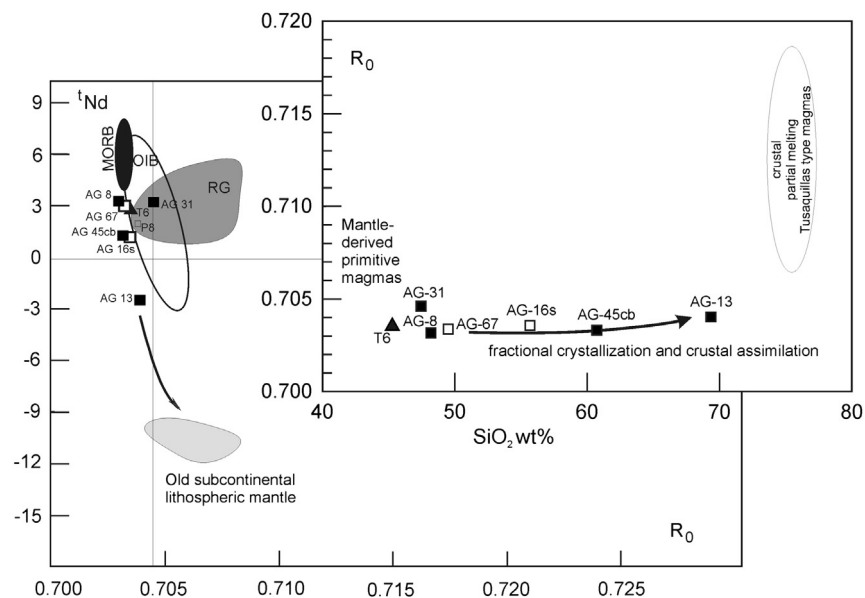
Fig. 8. A. Chondrite-normalized rare-earth elements patterns for Aguilar granitoid samples (squares), compared with the silicic Tusaquillas rocks (grey field) (Cristiani et al., 2005). B. Primitive mantle-normalized multi-elements patterns for the same samples as in A. C. Chondrite-normalized rare-earth elements diagram for Aguilar mafic rocks (squares, MgO from 4.4 to 6.9 wt.%), compared to sample T6 (triangles) of the Castro Tolay pluton (MgO = 13.24 wt.%) (Cristiani et al., 2005). D. Primitive mantle-normalized multi-elements pattern for the same samples as in C. Normalization values after Sun and McDonough (1989).
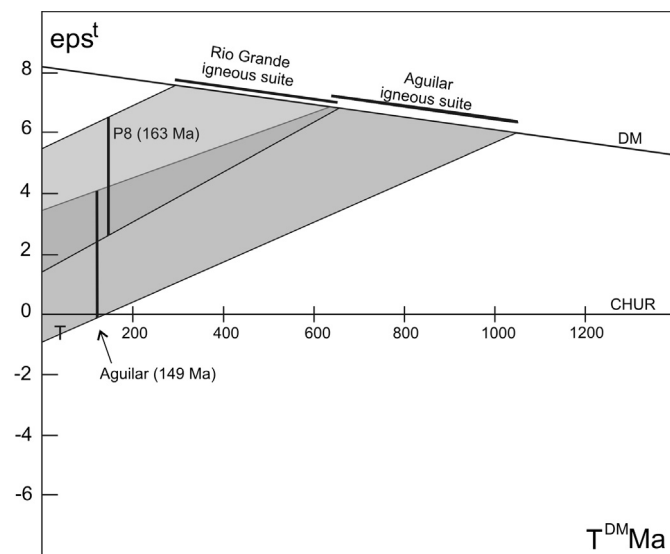
Fig. 9. Isotope evolution of epsNd against time for the Aguilar and Rio Grande igneous suites (c.f. DePaolo, 1988). See text for explanations.

crystallization involved mainly plagioclase, with biotite and alkali feldspar, and included apatite and Fe–Ti oxides.

The mineral chemistry obtained on AG samples is characteristic of alkaline plutons, as suggested by the high content of relatively sodic plagioclase and by the high FeO compared to MgO and Al_2O_3 of biotite (Abdel Rahman, 1994). Using the tectonic setting discriminant diagram proposed by Abdel-Rahman (1994) the analyzed biotite composition plots in the field of alkaline suites (Fig. 10A).

Biotite and hornblende are the dominant ferromagnesian minerals in the granitoid rocks of the AG pluton. We have examined the variation of Mg# [$Mg/(Mg + Fe^{2+})$ mol%] values for hornblende-biotite pairs in the diagram proposed by Poli and Tommasini (1991) (Fig. 10B). Considering samples with bulk rock SiO_2 content of 54–74 wt %, the Mg# values range from 0.45 to 0.25 in hornblende and from 0.35 to 0.25 in biotite. The hornblende-biotite pairs of samples AG18, AG45s and AG13 plot close to the 1:1 line suggesting crystallization under equilibrium conditions (Fig. 10B). In these samples the biotite and hornblende crystals have euhedral shape, confirming the equilibrium with the silicate melt. In contrast, the sample AG45ca lays outside of the 1:1 line, suggesting disequilibrium in the mineral-forming process which could be interpreted as a result of mixing between mafic (hornblende-bearing) and evolved (biotite-bearing) magmas. In this sample, the hornblende crystals have anhedral habitus and resorption textures, suggesting that they had crystallized in equilibrium with a different liquid. This is an evidence of mingling–mixing processes between magmas with different degree of evolution during the AG pluton emplacement and cooling.

Mingling–mixing processes are also indicated by the presence of magmatic microgranular enclaves (Fig. 3). We interpret these enclaves as the result of the arrival of new magma batches, with similar mantle source and moderately different evolutive history, in the already differentiated reservoir (e.g.; Poli and Tommasini, 1991; Bateman, 1995; Gagnevin et al., 2004; Harper et al., 2004; Pons et al., 2006; Riishuus et al., 2008; Barnes et al., 2009). Field observations of the rounded shapes of the enclaves and petrographic evidence of transfer of host-rock crystals to the enclaves and vice-versa imply mixing between the resident magma and a new influx of magma in the reservoir, with only partial hybridization (Fig. 3A–E). In some cases, the fine-grained groundmass of the mafic
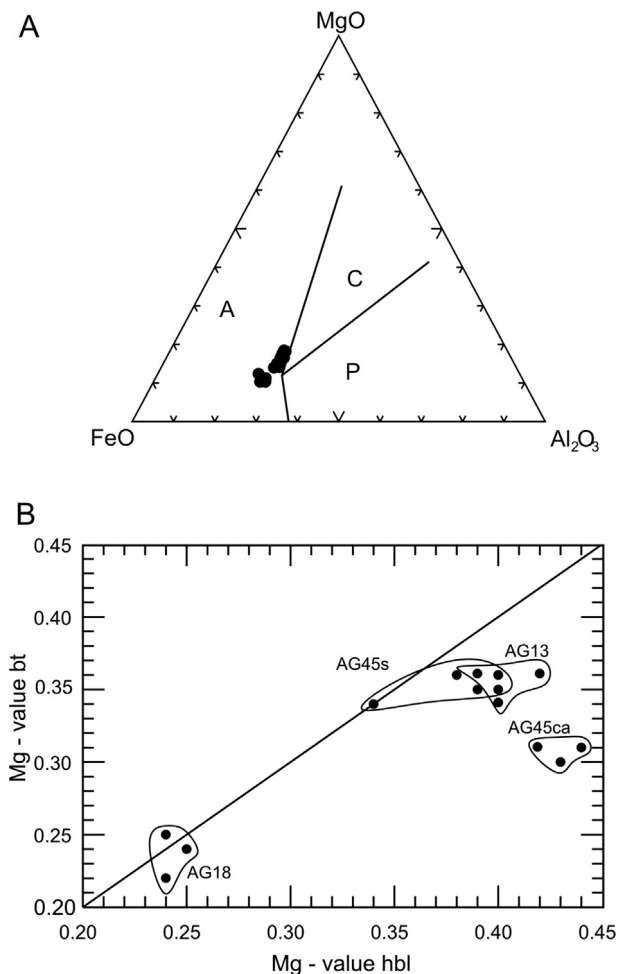

Fig. 10. A. Composition of biotite from Aguilar pluton reported in the tectonic setting discrimination diagram after Abdel-Rahman (1994). A: alkaline, C: calcalkaline, and P: peraluminous granite fields. B. Mg# [$Mg/(Mg + Fe^{2+})$ mol%] for hornblende-biotite pairs of the Aguilar pluton (after Poli and Tommasini, 1991). Samples: AG13 monzogranite ($SiO_2 = 69.41$ wt.%), AG18 monzogranite ($SiO_2 = 74.04$ wt.%), AG45ca quartz-syenite ($SiO_2 = 60.75$ wt.%), AG45s monzodiorite enclave ($SiO_2 = 53.54$ wt.%).

enclaves and their sharp contact with the biotite-hornblende monzogranite suggest a large temperature contrast between the two magmas (Fig. 3 C–D).

6.1.3. Temperature and pressure conditions of petrogenetic processes

In order to have inferences on the crystallization path of the AG rocks, the samples have been plotted in the residual granitic system Ks–Ne–Silica diagram (Fig. 11; Hamilton and Mackenzie, 1965). The data as a whole show a linear trend extending from the Ab-Or join (m2) towards the granite minimum (m1). The mafic samples mainly plot in the field between m2 and m3 minima. We have included in the diagram the peridotite xenoliths of Lucassen et al. (2005) and the most primitive rocks associated with the Jurassic-Early Cretaceous magmatism of NW Argentina, i.e. the Castro Tolay gabbro and the Rio Grande lamprophyric dykes.

Most AG rocks define a differentiation trend in the oversaturated part of the diagram. The trend originates from mafic magma composition close to the Ab-Or join. This differentiation interval covers a large SiO_2 range, 47–76 wt%, and is in agreement with the trends observed in the major and trace elements variation diagrams, showing an initial crystallization dominated by clinopyroxene and minor plagioclase, followed by clinopyroxene,
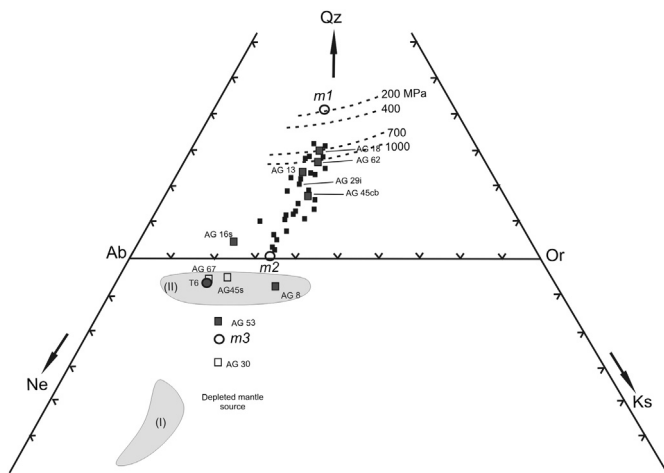
Fig. 11. Composition of AG samples reported into the Petrogeny's Residua Systems (Ks-Ne-Q wt.%) after Hamilton and McKenzie (1965), showing the liquid evolution path dominated by fractional crystallization. (I) primitive mantle source (Lucassen et al., 2002, 2005), (II) mafic alkaline magmas (data sources: Cristiani, 2003; Cristiani et al., 2005; Hauser et al., 2010). Granite minimum melt (*m1*), syenite minimum melt on the feldspar join (*m2*), and phonolite minimum melt (*m3*). The pressure-dependent field boundaries are compiled after Anderson and Culler (1978) and Anderson and Bender (1989).

plagioclase, biotite and hornblende. The most silica-rich samples ($SiO_2 = 74-76$ wt%) of biotite monzogranite and biotite-hornblende monzogranite can be considered representative of residual melts according to their chemical composition (Fig. S1 in Supplementary Files) and textural characteristic. These rocks plot close to the 600 MPa curve, suggesting that final crystallization of the magma occurred at about 18–20 km of depth. The pressure could be overestimated if the granite has cumulatic character, but this is not the case of AG pluton. Indeed, considering the mineral assemblage of the contact metamorphic aureole of the pluton (Fig. 2), the presence of andalusite-cordierite-biotite-feldspar-quartz hornfels indicates a depth of emplacement and cooling of the pluton at 12–15 km.

An estimate of the temperature of magma crystallization of the AG pluton can be quantitatively derived by using the Al-in-hornblende geo-thermobarometer (Blundy and Holland, 1990). The application of this thermobarometer requires the presence of the assemblage quartz + plagioclase + K-feldspar + hornblende + biotite + titanite + Fe–Ti oxide phases (Vyhnal et al., 1991). Fortunately, the felsic rocks (AG13, AG18, and AG45ca) contain the full mineral assemblage and the total aluminum variation in the hornblende crystals is low. The calculated temperatures indicate an average of 722 °C for the core and 713 °C for the rim of crystals. The values obtained using hornblende-plagioclase thermometer (Blundy and Holland, 1990) gave an average of 778 °C and 765 °C, respectively. In the biotite monzogranite and biotite-hornblende monzogranite, zirconium concentration regularly decreases, suggesting zircon saturation. The temperature estimated applying the zircon saturation thermometer is in the range 800–860 °C (Watson and Harrison, 1983). However, the temperatures estimated using the apatite saturation thermometer of Harrison and Watson (1984) on the same samples are higher than 850 °C. This discrepancy may be due to zircon or apatite cumulates in the rock (Frost et al., 1999). In summary, all these data indicate a crystallization temperature of the most evolved rocks of the AG pluton between 750 and 800 °C.

6.1.4. Pluton emplacement

The field and petrographic evidence of magma mingling and mixing events, the geochemical evidence of the presence of both silica-undersaturated and saturated mafic rocks in the pluton suggest that the AG pluton formed for the ascent, storage and crystallization of different magma batches. As a consequence, a small pluton formed in the upper crust, at shallow depth, with size on the order of few hundreds of cubic kilometers. The emplacement of a pluton of this size should have taken place in a relatively narrow span of time (De Saint Blanquat et al., 2011). The AG pluton can thus be envisaged as the cooling of a compositionally stratified magma chamber (Fig. 12A and B). The mafic bodies cropping out in the central-eastern zone of the AG pluton (El Quemado, valle de la Oriental and cerro Espejo, Fig. 2) could be interpreted as the injection-pipe zone of the mafic magmas into an already differentiated, but only partially crystallized, reservoir. The disrupted sill-like intrusions of intermediate composition have, probably, flowed laterally from the central zone, being denser than the resident magma. The swarms of diorite, monzodiorite and minor
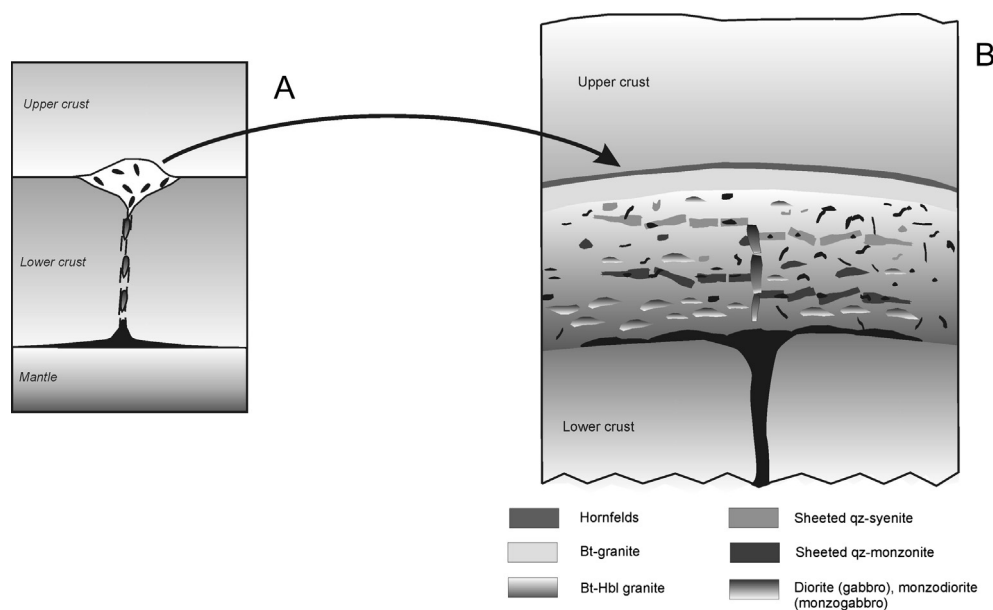

Fig. 12. Tentative reconstruction of the AG pluton emplacement as inferred from the field and petrologic data. See text for explanations.

gabbro enclaves (see Fig. 3) could be the result of more than one mafic inputs that disrupted into the silicic magma chamber. The thermal input derived from the recurrent injection of mafic magmas into the magmatic chamber could induce a local convective stirring favoring the development of the igneous banding (Pons et al., 2006). The close association of magmatic layering with the presence of enclaves of different size, shape, texture and composition in the biotite-hornblende monzogranite provides the evidence that these were formed when both, the resident silicic body and the mafic magma blobs, still had a plastic behavior, due to their incomplete solidification (Perugini et al., 2003; Gagnevin et al., 2004; Barbarin, 2005; Harper et al., 2004; Riishuus et al., 2008; Barnes et al., 2009). In contrast, the biotite monzogranite does not contain enclaves neither mafic bodies. We interpret the biotite monzogranite as the outer and upper portion of the magma chamber, characterized, at the time of magma mingling, by lower temperatures and thus higher solidification degree than the inner main part of the pluton, still hot and mostly molten.

In agreement, the presence of feldspar megacrysts with sieve-textured cores and anti-rapakivi-rims in the AG pluton can be related to thermal and chemical disequilibrium conditions in the magma chamber, originated by the mixing of magmas with contrasting compositions and volatile contents (Wark and Stimac, 1992; Castro, 2001; Pietranik and Waight, 2008; Alves et al., 2009).

In Fig. 12B we show a schematic interpretation of the emplacement structure of the AG pluton, taking into account the spatial distribution of its rock types. This structure could be the result of the following successive phases of intrusion in the final storage level in the shallow upper crust: a) emplacement of an initial batch of granitoid magma, undergoing cooling and solidification at the contact with the country rocks, where it formed the biotite monzogranite facies; b) mafic to intermediate magma infilling led to the expansion of the magmatic chamber and to mixing with the resident magma, producing sill-like intrusions and

several microgranular enclaves generations; thermal perturbation favored convection in the internal zone of the AG pluton and disruption of the sills, as well as plagioclase resorption; c) crystallization was, locally, controlled by different thermal conditions, causing the very different mingling textures observed in the pluton.

The new magma batches have a variable composition, from gabbro and diorite to monzodiorite, to syenite. This compositional range can only partially be due to hybridization during the mixing process. Instead, it suggests the existence of a deeper storage level, possibly at the base of the lower crust, where the mantle-derived melts reside and differentiate (Fig. 12A). This could explain the arrival of both silica-undersaturated and saturated magmas, as well as the fact that part of the mafic samples has already undergone substantial olivine fractionation, given their MgO and Ni contents.

In summary, on the base of all presented data, we propose that the AG pluton emplacement developed in two stages: (I) The parental magmas (mantle-derived basalt), generated in correspondence to ascending asthenospheric mantle, underwent some differentiation in correspondence of a first storage level, possibly at the base of the lower crust. (II) The differentiated magmas migrated through the crust with minor contamination and stopped in the attenuated crust at about 12–15 km of depth, probably at the boundary between the brittle upper crust and ductile middle-lower crust where tectonic traps can form (Fig. 12A). In this place, differentiation by fractional crystallization joined to crustal contamination, with a moderate decrease of the Nd isotope composition and a slight increase of the Sr isotope ratios, occurred (Fig. 8). New arrivals of mafic to intermediate magma batches from depth caused mixing and mingling processes.

6.2. The regional rift–related frame

The Late Jurassic-Early Cretaceous extensional phase occurred in NW Argentina in an intraplate position was marked by the
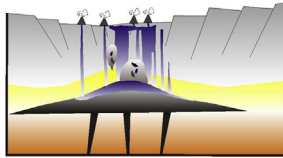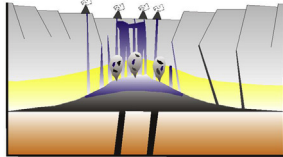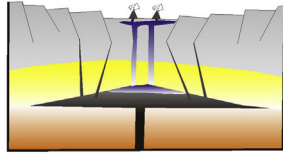

Period	Name	Main rock type	Age (Ma)	Regional geodynamic sketch model	Regional tectonic frame	^{t}Nd	R_0	References
135 Ma								
	Tusaquillas (23°12'03" S) (65°46'45" W)	bt- granite bt-mu granite	Rb/Sr 140 +/-1 144 +/-2	C	Progressive extension	-1.77 to 2.65	0.70867 to 0.722668	Zappettini (2008), Cristiani (2003), Cristiani et al. (2005)
	Aguilar (23°12'06" S) (65°41'56" W)	bt- granite bt-hbl granite qz-monzonite diorite/gabbro	Rb/Sr 149 +/-1 U/Pb 150.4 +/-0.9			-1.06 to 3.82	0.703198 to 0.704605	Cristiani (2003), Cristiani et al. (2005) Haschke et al. (2005)
JURASSIC	Castro Tolay (23°13'22" S) (65°41'43" W)	Gabbro, Diorite qz-syenite, monzogranite	Rb/Sr 150.6 +/-1 U/Pb 154.2 +/-0.92	B		-4.97 to 3.55	0.703545 to 0.713121	Zappettini (2008) Cristiani (2003), Cristiani et al. (2005)
	Abra Laite (23°12'03" S) (65°46'45" W)	bt- granite bt-mu granite	U/Pb 153 +/-4			-3.24 to -3.85	0.710668 to 0.713735	Cristiani (2003), Cristiani et al. (2005)
	Fundiciones (23°22'27" S) (65°26'53" W)	Syenite qz-syenite	U/Pb 160.4 +/-1.2 Ar/Ar 161.8 +/-2.7	A				Haschke et al. (2005)
175 Ma	Rio Grande (23°19'54" S) (65°26'37" W)	Lamprophyres	(bt) K/Ar 163 +/-9			5.61 to 1.52	0.70377 to 0.70781	Hauser et al. (2010)

Fig. 13. Conceptual evolutionary model of the Late Jurassic-Early Cretaceous magmatism of NW Argentina. Black to blue colours indicate magma differentiation. (For interpretation of the references to colour in this figure legend, the reader is referred to the web version of this article.)

emplacement in the crust of magmatic reservoirs with different petrological characteristics. These, presently, crop out as plutonic bodies, while the coeval volcanic products were mostly eroded (Fig. 13). The plutons are distributed across the Eastern Cordillera and Puna morphostructural provinces, extending for approximately 50 km from east to west (Fig. 1).

Overall, the intrusive rocks range in composition from slightly silica-undersaturated gabbros, (e.g.; Castro Tolay), to diorite to syenite and peralkaline syenite, metaluminous biotite-granite and biotite-hornblende granite, to peraluminous biotite-muscovite granite (e.g.; Tusaquillas) (Fig. 13). The small Aguilar pluton covers, alone, much of this compositional range.

On the basis of the available ages and compositional data of the intrusive suite, we envisage a three-stages tectono-magmatic evolution for this Jurassic extensional phase (see references in Fig. 13):

A. Lithospheric thinning promoted the genesis and emplacement of alkaline basaltic magma in an attenuated crust at the Moho level. The Rio Grande lamprophyric dykes, corresponding to very low degrees of partial melting, can be related to this initial stage (Hauser et al., 2010). This alkaline magmatism constrains the onset of the extensional phase in Late Jurassic time. Noteworthy, a NE-SW-elongate, strong residual positive gravimetric anomaly (Götze et al., 1994; Omarini et al., 1999) is coaxial with the dyke swarms generated during the initial stage of the rift formation.

B. With the increase of the extensional regime, moderately alkaline and transitional basaltic magmas were generated by slightly higher degrees of partial melting. Silica-undersaturated and saturated mafic magmas could have been generated at this stage (Castro Tolay and AG gabbroids). The primitive magmas differentiated by fractional crystallization and interaction with the crust, leading to the emplacement of alkaline to metaluminous granitoids.

C. At the Jurassic-Cretaceous boundary, silicic magmas, with minor volumes of mafic ones, were emplaced as plutonic bodies and dykes. The presence of peraluminous magmas with crustal isotopic signature suggests partial melting of the continental crust (Tusaquillas granite). Crustal melting could have been induced by the thermal perturbation due to asthenosphere upraise.

The compositional range of the plutonic suite, spanning from peralkaline to peraluminous rocks, is in agreement with an intraplate setting. Indeed, the geological position east of the Tarapacá backarc basin and the igneous rocks affinity exclude a subduction-related magma genesis. Instead, the above reconstruction envisages a rift-related frame for the Jurassic magmatism in NW Argentina. The Jurassic extensional phase can represent the early phase for the Cretaceous Salta rift. The large compositional heterogeneity of the AG pluton, emplaced in the above described frame, well fits in the proposed reconstruction.

7. Conclusions

The discussion of the geological, petrographic-mineralogical, geochemical and isotopic results on the Aguilar pluton rocks leads to the following conclusions:

1. Aguilar is a small intrusion composed of monzogranite rocks for over 80% of the outcropping pluton and of minor intermediate and mafic rocks. The granite has ferroan, alkalic to alkali-calcic composition, ranging from quartz-monzonite and

quartz-syenite to monzogranite. The mafic rocks are moderately alkaline, rarely slightly silica-undersaturated.

2. The plutonic complex is an example of a multistage mafic to felsic intrusion strongly affected by magma mingling and mixing events. We propose a model in which sill-like "magma sheets" of mafic to intermediate composition repeatedly intruded and disrupted into the cooling silicic magma chamber, forming the observed mixing and mingling features (gabbroid bodies and mafic enclaves in the hornblende-biotite granitoid, compositional and textural disequilibria in the mineral phases). The magma chamber was already partially crystallized at the boundary with the host rock. The outermost layer of silicic magma, largely solidified, was not reached by the mingling/mixing events and formed the present biotite-bearing monzogranite facies.

3. The rock suite was originated by differentiation of mantle-derived magmas by fractional crystallization and moderate crustal assimilation. The final emplacement in the upper crust, probably at the boundary with the middle crust, occurred at approximately 12–15 km of depth. A hornfels metamorphic aureole and calc-silicate skarns are associated to the pluton.

4. The age of AG pluton (150–149 Ma) is well within the age range of the other intrusive complexes emplaced in NW Argentina, east of the active continental margin, in an intraplate position, during the Late Jurassic-Early Cretaceous extensional phase. The geological position east of the Tarapacá backarc basin and the igneous rocks affinity exclude a subduction-related magma genesis. The available age and compositional data on the entire plutonic suite allow proposing a reconstruction coherent with the early stages of rift evolution. The compositional heterogeneity characterizing the magmas that formed the AG pluton well fits in the proposed reconstruction.

5. The geochemical data indicate that AG primitive magmas were derived from partial melting of a pristine Proterozoic mantle reservoir that was different from the Rio Grande alkaline reservoir, which represented the mantle source in the incipient stage of rift formation.

Appendix A. Supplementary data

Supplementary data related to this article can be found at http://dx.doi.org/10.1016/j.jsames.2013.06.002.

References

Abdel-Rahman, A.M., 1994. Nature of biotites from alkaline, calcalkaline and per-aluminous magmas. Journal of Petrology 35, 525–541.

Acocella, V., Vezzoli, L., Omarini, R., Matteini, M., Mazzuoli, R., 2007. Kinematic variations across Eastern Cordillera at 24°S (Central Andes): tectonic and magmatic implications. Tectonophysics 434 (1–4), 81–92.

Allmendinger, R.W., Zapata, T.R., 2000. The footwall ramp of the Subandean decollement, northernmost Argentina, from extended correlation of seismic reflection data. Tectonophysics 321, 37–55.

Alves, A., Janasi, V., Simonetti, A., Heaman, L., 2009. Microgranitic enclaves as products of self-mixing events: a study of open-system processes in the Maua

Granite, Sao Paulo, Brazil, based on in situ isotopic and trace elements in plagioclase. Journal of Petrology 50, 2221–2247.

Anderson, J.L., Culler, R.L., 1978. Geochemistry and evolution of the Wolf river batholith, a Late Precambrian rapakivi massif in North Wisconsin, U.S.A. Precambrian Research 7, 287–324.

Anderson, F.L., Bender, E.E., 1989. Nature and origin of Proterozoic A-Type granite magmatism in the southwestern United States of America. Lithos 23, 1952.

Bailey, S.W., 1984. Classification and structures of the micas. Crystal chemistry of the true micas. Reviews in Mineralogy, Mineralogical Society of America 13, 1–60.

Barbarin, B., 2005. Mafic magmatic enclaves and mafic rocks associated with some granitoids of the central Sierra Nevada batholith, California: nature, origin, and relations with the hosts. Lithos 80, 155–177.

Barnes, C.G., Prestvik, T., Li, Y., McCulloch, L., Yoshinobu, A.S., Frost, C.D., 2009. Growth and zoning of Hortavaer intrusive complex, a layered alkaline pluton in Norwegian Caledonides. Geosphere 5, 286–301.

Bateman, R., 1995. The interplay between crystallization, replenishment and hybridization in large felsic magma chambers. Earth Science Reviews 39, 91–106.

Blundy, J.D., Holland, T.J.B., 1990. Calcic amphibole equilibria and a new amphibole-plagioclase geothermometer. Contributions to Mineralogy and Petrology 104, 208–224.

Bonin, B., 2007. A-type granites and related rocks: evolution of a concept, problems and prospects. Lithos 97, 1–29.

Brodtkorb, M.K., Lanfranco, J.J., Sureda, R., 1978. Asociaciones mineralogicas y litologia del yacimiento Aguilar, Prov. de Jujuy, República Argentina. Asociación Geologica Argentina 33, 277–298.

Boekhout, F., Spikings, R., Sempere, T., Chiaradia, M., Ulianov, A., Schaltegger, U., 2012. Mesozoic arc magmatism along the southern Peruvian margin during Gondwana breakup and dispersal. Lithos 146–147, 48–64.

Castro, A., 2001. Plagioclase morphologies in assimilation experiments. Implications for disequilibrium melting in the generation of granodiorite rocks. Mineralogy and Petrology 71, 31–49.

Charrier, R., Muñoz, N., 1994. Jurassic-Cretaceous palaeogeographic evolution of the Chilian Andes at 23°24′S Latitude and 34°35′S Latitude: a comparative analisis. In: Reutter, K.J., Scheuber, E., Wigger, P.J. (Eds.), Tectonics of the Southern Central Andes. Springer-Verlag, pp. 33–243.

Cladouhos, T.T., Allmendinger, R.W., Coira, B., Farrar, E., 1994. Late Cenozoic deformation in the Central Andes: fault kinematics from the northern Puna, northwestern Argentina and southwestern Bolivia. Journal of South American Earth Sciences 7, 209–228.

Comin-Chiaramonti, P., Lucassen, F., Girardi, V.A.V., De Min, A., Gomes, C.B., 2009. Lavas and their mantle xenoliths from intracratonic Eastern Paraguay (South America Platform) and Andean Domain, NW-Argentina: a comparative review. Contribution to Mineralogy and Petrology 98, 143–165.

Coutand, I., Cobbold, P.R., de Urreiztieta, M., Gautier, P., Chauvin, A., Gapais, D., Rossello, E.A., Lopez-Gamundi, O., 2001. Style and history of Andean deformation, Puna plateau, northwestern Argentina. Tectonics 20, 210–234.

Cristiani, C., 2003. Il plutonismo anorogenico Mesozoico nell' Altipiano della Puna (Argentina Nord-occidentale, Ande Centrali): implicazioni petrogenetiche e geodinamiche (PhD thesis). University of Pisa, Italy, p. 229.

Cristiani, C., Matteini, M., Mazzuoli, R., Omarini, R., 2002. Geochemical characters of the Aguilar and Tusaquillas plutonic complexes (NW Argentina): insights on the genesis and evolution of the magmas during the Jurassic–Cretaceous continental rift. In: XV Congreso Geológico Argentino, Neuquén, vol. 2, pp. 168–171.

Cristiani, C., Matteini, M., Mazzuoli, R., Omarini, R., 2003. Petrological study of interaction processes between crustal and mantle magmas for reconstructing the geotectonic setting a continental rift: case of Jurassic-Cretaceous Tusaquillas plutonic complex in Central Andes (NW Argentina). Geophysical Research Abstracts 5, 12577.

Cristiani, C., Matteini, M., Mazzuoli, R., Omarini, R., Villa, I.M., 2005. Petrology of Late Jurassic-Early Cretaceous Tusaquillas and Abra Laite-Aguilar Plutonic complexes (Central Andes, 23°05′ S–66°05′W): a comparison with the rift-related magmatism of NW Argentina and E Bolivia. In: Comin-Chiaramonti, P., Barros Gomez, C. (Eds.), Mesozoic to Cenozoic Alkaline Magmatism in the Brazilian Plataform. Editora da Universidade de São Paulo, Brazil, ISBN 85-314-0903-9, pp. 213–241.

De Saint Blanquat, M., Horsman, E., Habert, G., Morgan, S., Vanderhaeghe, O., 2011. Multiscale magmatic cyclicity, duration of pluton construction, and the paradoxical relationship between tectonism and plutonism in continental arcs. Tectonophysics 500, 20–33.

DePaolo, D., 1988. Trace element and isotopic effects of combined wallrock assimilation and fractional crystallization. Earth and Planetary Science Letters 53, 189–202.

Drozdzewski, G., Mon, R., 1999. Oppositely-verging thrusting structures in the North Argentine Andes compared with the German Variscides. Acta Geologica Hispanica 34, 185–196.

Escayola, M.P., van Staal, C.R., Davies, W.J., 2011. The age and tectonic setting of the Puncoviscana Formation in northwestern Argentina: an accretionary complex related to Early Cambrian closure of the Puncoviscana Ocean and accretion of the Arequipa-Antofalla block. Journal of South American Earth Science 30, 1–22.

Frost, C.D., Frost, R.B., Chamberlain, K.R., Edwards, B.R., 1999. Petrogenesis of the 1.43 Ga Sherman Batholith, SE Wyoming, USA: a Reduced, Rapakivi-type Anorogenic Granite. Journal of Petrology 40, 1771–1802.

Frost, R.B., Calvin, G., Barnes, W.J., Collins, R.J., Arculus, D.J., Frost, C.D., 2001. A geochemical classification for granitic rocks. Journal of Petrology 42, 2033–2048.

Frost, C.D., Frost, R.B., 2011. On ferroan (A-type) granitoids: their compositional variability and modes of origin. Journal of Petrology 52, 39–53.

Gagnevin, D., Daly, J.S., Poli, G., 2004. Petrographic, geochemical and isotopic constraints on magma dynamics and mixing in the Miocene Monte Capanne monzogranite (Elba Island, Italy). Lithos 78, 157–195.

Gemmell, J.B., Zantop, H., Meinert, L.D., 1992. Genesis of the Aguilar zinc-lead-silver deposit, Argentina: contact metasomatic vs. sedimentary exhalative. Economic Geology 87, 2085–2112.

Giret, A., Bonin, B., Leger, J.M., 1980. Amphibole compositional trends in oversaturated and undersaturated alkaline plutonic ring-complexes. Canadian Mineralogist 18, 481–495.

Götze, H.J., Schmidt, S., Strunk, S., 1994. The lithospheric structure of the Central Andes (20°–26° S) as inferred from interpretations of regional gravity. In: Reutter, K.J., Scheuber, E., Wigger, P.J. (Eds.), Tectonics of the Southern Central Andes. Springer, pp. 79–123.

Gröschke, M., von Hillebrandt, A., Prinz, P., Quinzio, L.A., Wilke, H.G.l, 1988. Marine Mesozoic Peleogeography in northern Chile between 21°–26° S. In: Bahlburg, H., Breitkreuz, Ch., Giese, P. (Eds.), The Southern Central Andes, Lecture Notes in Earth Sciences, vol. 17. Springer-Verlag, pp. 105–117.

Halpern, M., Latorre, C.O., 1973. Estudio geocronológico inicial de rocas del noroeste de la República Argentina. Revista de la Asociación Geológica Argentina 28, 195–205.

Hamilton, D.L., Mackenzie, W.S., 1965. Phase equilibrium studies in the system $NaAlSiO_4$–$KAlSiO_4$–SiO_2–H_2O. Mineralogical Magazine 34, 214–231.

Harper, B.E., Miller, C.F., Koteas, G.C., Cates, N.L., Wiebe, R.A., Lazzareschi, D.S., Gribb, J.W., 2004. Granite dynamic magma chamber processes and pluton construction: the Aztec Wash pluton, Eldorado Mountains, Nevada, USA. Royal Society of Edinburgh Transactions, Earth Sciences 95, 277–295.

Harrison, T.M., Watson, E.B., 1984. The behavior of apatite during crustal anatexis: equilibrium and kinetic considerations. Geochimica et Cosmochimica Acta 48, 1467–1477.

Haschke, M., Deeken, A., Insem, N., Sobel, E., Grove, M., Schmitt, A.K., 2005. Growth pattern of the Andean Puna Plateau constrained by apatite fission track, apatite (U–Th)/He, K-feldspar $^{40}Ar/^{39}Ar$, and zircon U–Pb geochronology. In: Andean Geodynamics, Extended Abstracts. ISAG, Paris, pp. 360–363. International Symposium on Andean Geodynamics, 2006, Barcelona.

Hausen, J., 1925. Sobre un perfil geológico del borde oriental de la Puna de Atacama. Academia Nacional de Ciencias de Bolivia 28, 1–96.

Hauser, N., Matteini, M., Omarini, R.H., Pimentel, M.M., 2010. Constraints on metasomatized mantle under Central South America: evidence from Jurassic alkaline lamprophyre dyke from Eastern Cordillera, NW Argentina. Mineralogy and Petrology 100, 153–184.

Hauser, N., Matteini, M., Omarini, R.H., Pimentel, M.M., 2011. Combined U–Pb and Lu–Hf isotope data on turbidites of the Paleozoic basement of NW Argentina and petrology of associated igneous rocks: implications for the tectonic evolution of western Gondwana between 560 and 460 Ma. Gondwana Research 19, 100–127.

Hibbard, M.J., 1981. The magma mixing origin of mantled feldspar. Contributions to Mineralogy and Petrology 76, 158–170.

Irvine, T.N., Baragar, W.R.A., 1971. A guide to chemical classification of the common rocks. Canadian Journal of Earth Science 8, 523–548.

Jaillard, E., Soler, P., Carlier, G., Mourier, T., 1990. Geodynamic evolution of the northern and central Andes during early to middle Mesozoic time: a Tethyan model. Journal of Geological Society of London 147, 1009–1022.

Jaillard, E., Hérail, G., Monfret, T., Díaz-Martínez, E., Baby, P., Lavenu, A., Mumont, J.F., 2000. Tectonic evolution of the Andes of Ecuador, Peru, bolivia and northernmost Chile. In: Cordani, U.G., Milani, E.J., Filho, Thomaz, Campos, D.A. (Eds.), Tectonic Evolution of South America. 31st. Internationa Geological Congress, Brazil, pp. 481–559.

Kley, J., Monaldi, C.R., Salfity, J.A., 1999. Along-strike segmentation of the Andean foreland: causes and consequences. Tectonophysics 301, 75–94.

Lamfranco, J., 1972. Estudio de la intrusión en la falda oriental de la Sierra de Aguilar y metamorfitas del area de contacto (PhD thesis). Universidad Nacional de Córdoba, Argentina, p. 202.

Leake, B.E., Woolley, A.R., Arps, C.E.S., et al., 1997. Nomenclature of amphiboles: report of the subcommittee on amphiboles of the International Mineralogical Association, Commission on New Minerals and Mineral Names. The Canadian Mineralogist 35, 219–246.

Le Maitre, R.W., Bateman, P., Dudek, A., Keller, J., Lamayre Le Bas, M.J., Sabine, P.A., Schmid, R., Sorensen, H., Strekeisen, A., Woolley, A.R., Zanettin, B., 1989. Classification of Igneous Rocks and Glossary of Terms. Blackwell, Scientifics Publications, Oxford, p. 193.

Linares, E., 1968. Geología isotópica del azufre del Yacimiento Aguilar, provincia de Jujuy. In: I. II Jornadas Geológicas Argentina, Actas, vol. 2, pp. 191–199.

Linares, E., Latorre, C.O., 1975. La edad del Granito de El Aguilar, Provincia de Jujuy. In: Actas II Congreso Iberoamericano de Geologia Economica, Buenos Aires, vol. 1, pp. 91–98.

Lucassen, F., Lewerenz, S., Franz, G., Viramonte, J., Mezger, K., 1999. Metamorphism isotopic ages and composition of lower crustal granulite xenoliths from cretaceous Salta Rift. Argentina. Contributions to Mineralogy and Petrology 134, 325–341.

Lucassen, F., Escayola, M., Franz, G., Romer, R.L., Koch, K., 2002. Isotopic composition of late Mesozoic basic and ultrabasic rocks from Andes, 23–32° S) – implications for the Andean mantle. Contributions to Mineralogy and Petrology 143, 336–349.

Lucassen, F., Franz, G., Viramonte, J., Romer, R.L., Dulski, P., Lang, A., 2005. The late Cretaceous lithospheric mantle beneath the Central Andes: evidence from phase equilibrium and composition of mantle xenoliths. Lithos 82, 379–406.

Lucassen, F., Franz, G., Romer, R.L., Schultz, F., Dulski, P., Wemmer, K., 2007. Pre-Cenozoic intra-plate magmatism along the Central Andes (17–34°S): composition of the mantle at an active margin. Lithos 99, 312–338.

Marquillas, R., Salfity, J.A., 1988. Tectonic framework and correlations of the Cretaceous-Eocene Salta Group, Argentina. In: Bahlburg, H., Breitkreuz, Ch., Giese, P. (Eds.), The Southern Central Andes, Lecture Notes in Earth Sciences, vol. 17. Springer-Verlag, pp. 119–136.

Marrett, R.A., Strecker, M.R., 2000. Response of intracontinental deformation in the Central Andes to late Cenozoic reorganization of South American Plate motions. Tectonics 19, 452–467.

Menegatti, N., 2001. El Complejo Alcalino Sierra de Rangel, Provincia de Salta, Argentina (PhD thesis). Universidad Nacional de Salta, Argentina, p. 157.

Middlemost, E.A.K., 1994. Naming materials in magma/igneous rock system. Earth Science Reviews 37, 215–224.

Morimoto, N., 1988. Nomenclature of pyroxenes. Mineralogical Magazine 52, 535–550.

Mpodozis, C., Ramos, V.A., 1990. The Andes of Chile and Argentina. In: Ericksen, G.E., Cañas Pinochet, M.T., Reinemuf (Eds.), Geology of the Andes and Its Relation to Hydrocarbon and Mineral Resources, Earth Sciences Series, vol. 1. Circumpacific Council for Energy and Mineral Resources, pp. 59–90.

Muñoz, N., Venegas, R., Téllez, C., 1988. La Formación La Negra: Nuevos antecedentes estratigráficos en la Cordillera de la Costa de Antofagasta. In: V Congreso Geologico Chileno, Santiago, vol. 1, pp. 283–311.

Oliveros, V., Féraud, G., Aguirre, L., Fornari, M., Morata, D., 2006. The early Andean magmatic province (EAMP): $^{40}Ar/^{39}Ar$ dating on Mesozoic volcanic and plutonic rocks from the Coastal Cordillera, Northern Chile. Journal of Volcanology and Geothermal Research 157, 311–330.

Omarini, R.H., Sureda, R.J., Götze, J.H., Seilacher, A., Pflüger, F., 1999. Puncoviscana folded belt in northwestern Argentina: testimony of Late Proterozoic Rodinia fragmentation and pre-Gondwana collisional episodes. International Journal of Earth Sciences 88, 76–97.

Perugini, D., Poli, G., Christofides, G., Eleftheriadis, G., 2003. Magma mixing in the Sithonia Complex, Greece: evidence from mafic microgranular enclaves. Mineralogy and Petrology 78, 173–200.

Pietranik, A., Waight, T.E., 2008. Processes and sources during Late Variscan dioritic-tonalitic magmatism: insights from plagioclase chemistry (Gesiniec Intrusion, NE Bohemian Massif, Poland). Journal of Petrology 49, 1619–1645.

Poli, G., Tommasini, S., 1991. Model for the origin and significance of Microgranular Enclaves in calc-alkaline granitoids. Journal of Petrology 32, 657–666.

Pons, J., Barbey, P., Nachit, H., Burg, J.P., 2006. Development of igneous layering during growth of pluton: the Tarcouate Laccolith (Morocco). Tectonophysics 413, 271–286.

Printz, P., Wilke, H.G., Hillebrand, A.V., 1994. Sediment accumulation and subsidence history in the Mesozoic marginal basin of Northern Chile. In: Reutter, K.J., Scheuber, E., Wigger, P.J. (Eds.), Tectonics of the Southern Central Andes. Springer, pp. 219–233.

Ramos, V.A., 2000. The southern central Andes. In: Cordani, U.G., Milani, E.J., Filho, Thomaz, Campos, D.A. (Eds.), Tectonic Evolution of South America. 31st. International Geological Congress, Brazil, pp. 561–604.

Ramos, V.A., 2009. Anatomy and Global Context of the Andes: Main Geologic Features and the Andean Orogenic Cycle. In: The Geological Society of America Memoir, vol. 204, pp. 31–65.

Riishuus, M.S., Peate, D.W., Tegner, C., Wilkson, J.R., Brooks, C.K., 2008. Petrogenesis of cogenetic silica-oversaturated and undersaturated syenite by periodic recharge in a crustally contaminated magma chamber: the Kangerlussuaq Intrusion, East Greenland. Journal of Petrology 49, 493–522.

Rubiolo, D.G., 1992. Clausthaler Geowissenchaftliche Dissertationen. Zur Geologie, Petrographie und Geochemie der Acali Magmatite der Sierra de Santa Victoria (E-Kordillere, NW-Argentinien), vol. 41, p. 145.

Rutland, R.W.R., 1971. Andean orogeny and sea floor spreading. Nature 233, 252–255.

Salfity, J., Marquillas, R., 1994. Tectonic and sedimentary evolution of the Cretaceous-Eocene Salta Group basin, Argentina. In: Salfity, J.A. (Ed.), Cretaceous Tectonics of the Andes. Braunschweig/Wiesbaden, Earth Evolution Sciencies, Monograph. Series, pp. 266–315.

Scheuber, E., Bogdanic, T., Jensen, A., Reutter, K.J., 1994. Tectonic development of the North Chilean Andes in relation to plate convergence and magmatism since Jurassic. In: Reutter, K.J., Scheuber, E., Wigger, P.J. (Eds.), Tectonics of Southern Central Andes. Structure and Evolution of an Active Continental Margin. Springer-Verlag, Berlin, pp. 121–139.

Sempere, T., Carlier, G., Soler, P., Fornari, M., Carlotto, V., Jacay, J., Arispe, O., Néraudeau, D., Cárdenas, J., Rosas, S., Jimenéz, N., 2002. Late Permian-middle Jurassic lithospheric thinning in Peru and Bolivia, and its bearing on Andean-age tectonics. Tectonophysics 345, 153–181.

Słaby, E., Götze, J., 2004. Feldspar crystallization under magma-mixing conditions shown by cathodoluminescence and geochemical modeling: a case study from the Karkonosze pluton (SW Poland). Mineralogical Magazine 68, 561–577.

Spencer, F.N., 1950. The geology of the Aguilar lead-zinc mine Argentina. Economic Geology 45, 405–433.

Stern, C.R., 1991. Role of subduction erosion in the generation of the Andean magmas. Geology 19, 78–81.

Stipanicic, L.N., Linares, E., 1969. Edades radimétricas determinadas para la Repúplica Argentina y su significado geológico. Academia Nacional de Ciencias de Córdoba, Boletín 47, 51–96.

Streickeisen, A., 1976. To each plutonic rocks its proper name. Earth Science Reviews 12, 1–32.

Sun, S.S., McDonough, W.F., 1989. Chemical and isotopic systematics of oceanic basalt: implications for mantle composition and processes. In: Saunders, A.D., Norry, M.J. (Eds.), Magmatism in Ocean Basins, Geological Society of London Special Publication, pp. 313–345.

Sureda, R.J., Martín, J.L., 1990. El Aguilar Mine: an Ordovician sediment-hosted stratiform lead-zinc deposit in the Central Andes. In: Fontbotè, L., Amstutz, G., Cardozo, E., Cedillo, E. (Eds.), Stratabound Ore Deposits in the Andes. Springer-Verlag, pp. 161–174.

Turner, J.C.M., 1970. The Andes of Northwestern Argentina. Geologische Rundschau 59, 1028–1063.

Vance, J.A., 1965. Zoning in igneous plagioclase: patchy zoning. Journal of Geology 73, 636–651.

Viramonte, J.G., Kay, S.M., Becchio, R., Escayola, M., Novitski, I., 1999. Cretaceous rift related magmatism in central-western South America. Journal of South American Earth Science 12, 109–121.

Vyhnal, C.R., NcSween, H.Y., Speer, J.A., 1991. Hornblende chemistry in southern Appalachian granitoids: implications for aluminum in hornblende thermobarometry and magmatic epidote stability. American Mineralogist 76, 176–188.

Wark, D.A., Stimac, J.A., 1992. Origin of mantled (rapakivi) feldspars: experimental evidence of a dissolution- and diffusion-controlled mechanism. Contributions to Mineralogy and Petrology 111, 345–361.

Watson, E.M., Harrison, T.M., 1983. Zircon saturation revisited: temperature and compositional effects in a variety of crustal magma types. Earth and Planetary Science Letters 64, 295–304.

Zappettini, E.O., 2008. El Plutonismo Mesozoico en Jujuy. In: Coira, B., Zappettini, E.O. (Eds.), Geología y Recursos Naturales de la Provincia de Jujuy, Relatorio XVII Congreso Geologico Argentino, pp. 244–257.

Zindler, A., Hart, S., 1986. Chemical geodynamics. Annual Review of Earth and Planetary Sciences 14, 493–571.

Zonenshayn, L.P., Savotin, L.A., Sedov, A.P., 1984. Global paleogeodynamic reconstructions for the last 160 million years. Geotectonics 18, 181–195.